

1 **Global and zonal-mean hydrological response to early Eocene**
2 **warmth**

3
4 Margot J. Cramwinckel^{1,#}, Natalie J. Burls², Abdullah A. Fahad^{2,3}, Scott Knapp², Christopher
5 K. West^{4,5,&}, Tammo Reichgelt⁶, David R. Greenwood⁷, Wing-Le Chan⁸, Yannick
6 Donnadieu⁹, David K. Hutchinson¹⁰, Agatha M. de Boer¹¹, Jean-Baptiste Ladant¹², Polina A.
7 Morozova¹³, Igor Niezgodzki^{14,15}, Gregor Knorr¹⁵, Sebastian Steinig¹⁶, Zhongshi Zhang¹⁷,
8 Jiang Zhu¹⁸, Ran Feng¹⁹, Daniel J. Lunt¹⁶, Ayako Abe-Ouchi⁸, and Gordon N. Inglis^{1*}

9
10 ¹School of Ocean and Earth Science, University of Southampton, Southampton, United
11 Kingdom

12 ²Department of Atmospheric, Oceanic and Earth Sciences, Center for Ocean-Land-
13 Atmosphere Studies, George Mason University, Fairfax, USA

14 ³GMAO, NASA Goddard Space Flight Center, Greenbelt, MD, USA

15 ⁴Department of Earth and Atmospheric Sciences, University of Alberta, Edmonton, Canada

16 ⁵Royal Tyrrell Museum of Palaeontology, Drumheller, Alberta, Canada

17 ⁶Department of Geosciences, University of Connecticut, Storrs, USA

18 ⁷Department of Biology, Brandon University, Brandon, Canada

19 ⁸Atmosphere and Ocean Research Institute, University of Tokyo, Japan

20 ⁹Laboratoire des Sciences du Climat et de l'Environnement, France

21 ¹⁰Climate Change Research Centre, University of New South Wales Sydney, Australia

22 ¹¹Department of Geological Sciences, Stockholm University, Sweden

23 ¹²Earth and Environmental Sciences, University of Michigan, US

24 ¹³Institute of Geography, Russian Academy of Sciences, Russia

25 ¹⁴Institute of Geological Sciences Polish Academy of Sciences, Kraków, Poland

26 ¹⁵Alfred Wegener Institute for Polar and Marine Research, Germany

27 ¹⁶School of Geographical Sciences, University of Bristol, UK

28 ¹⁷Bjerknes Centre for Climate Research, University of Bergen, Norway

29 ¹⁸National Center For Atmospheric Research, USA

30 ¹⁹Department of Earth Sciences, University of Connecticut, USA

31 [#]Now at: Department of Earth Sciences, Utrecht University, Utrecht, The Netherlands

32 [&]Now at: Royal Tyrrell Museum of Palaeontology, Alberta, Canada

33

34 *Corresponding author. Email: gordon.inglis@soton.ac.uk

35

36 **Abstract**

37 Earth's hydrological cycle is expected to intensify in response to global warming, with a 'wet-
38 gets-wetter, dry-gets-drier' response anticipated over the ocean. Subtropical regions (~15-
39 30°N/S) are predicted to become drier, yet proxy evidence from past warm climates
40 suggests these regions may be characterised by wetter conditions. Here we use an
41 integrated data-modelling approach to reconstruct global and zonal-mean rainfall patterns
42 during the early Eocene (~48-56 million years ago). The DeepMIP model ensemble indicates
43 that the mid- (30-60° N/S) and high-latitudes (>60° N/S) are characterised by a
44 thermodynamically-dominated hydrological response to warming and overall wetter
45 conditions. The tropical band (0-15° N/S) is also characterised by wetter conditions, with
46 several DeepMIP models simulating narrowing of the Inter-Tropical Convergence Zone
47 (ITCZ). Crucially, the latter is not evident from the proxy data. The subtropics are
48 characterised by negative precipitation-evaporation anomalies (i.e., drier conditions) in the
49 DeepMIP models, but there is surprisingly large inter-model variability in mean annual
50 precipitation. We find that models with weaker meridional temperature gradients (e.g.,
51 CESM, GFDL) are characterised by a reduction in subtropical moisture divergence, leading
52 to an increase in mean annual precipitation. Crucially, these model simulations agree more
53 closely with our new proxy-derived precipitation reconstructions and other key climate
54 metrics. This implies the early Eocene was characterised by reduced subtropical moisture

55 divergence. If the meridional temperature gradient was even weaker than suggested by
56 those DeepMIP models, circulation-induced changes may have outcompeted
57 thermodynamic changes, leading to wetter subtropics. This highlights the importance of
58 accurately reconstructing zonal temperature gradients when reconstructing past rainfall
59 patterns.

60

61 **Key points:**

- 62 • The early Eocene hydrological cycle in the DeepMIP models is characterised by
63 'wet-gets-wetter, dry-gets-drier' response over the ocean
- 64 • The early Eocene exhibits weaker subtropical moisture divergence in simulations
65 with reduced meridional temperature gradients
- 66 • Models with weaker meridional temperature gradients better simulate terrestrial-
67 derived precipitation estimates
- 68 • This highlights the important role of the meridional temperature gradient when
69 predicting past (and future) rainfall patterns
- 70 • However, DeepMIP models underestimate MAP estimates in the subtropics and mid-
71 to-high latitudes and overestimate MAP in the deep tropics

72

73 **1 Introduction**

74 Future global warming is projected to be associated with a global-mean increase in mean
75 annual precipitation (MAP) and a shift in regional and seasonal rainfall patterns (Chapter 8 of
76 Masson-Delmotte et al., 2022), with important consequences for societies and ecosystems.
77 Under higher global temperatures, Earth's atmosphere will contain more water vapour
78 following the Clausius–Clapeyron relation (Held and Soden, 2006). This 'thermodynamic
79 effect' forms the basis for the predicted zonal-mean "wet-gets-wetter, dry-gets-drier"
80 response under enhanced radiative forcing, whereby the existing spatial patterns in
81 precipitation-evaporation ($P-E$) are exacerbated over the ocean (Held and Soden, 2006;

82 Seager et al., 2010). However, this simple thermodynamic scaling does not hold true land
83 (Byrne and O’Gorman, 2015) and dynamical processes may also play an important role
84 (Byrne and O’Gorman, 2015). Overall, general circulation models (GCMs) used in Coupled
85 Model Intercomparison Project Phase 6 (CMIP6) suggest that higher global mean surface
86 temperatures (GMST) will lead to wetter high latitudes ($> 60^{\circ}\text{N/S}$) (i.e., positive $P-E$
87 change), and drier subtropics ($15-30^{\circ}\text{N/S}$) (i.e., negative $P-E$ change) (Hoegh-Guldberg et
88 al., 2018; Masson-Delmotte et al., 2022). However, the same models disagree on the nature
89 of change in much of the remainder of the low to middle latitudes, both over land and ocean
90 (Slingo et al., 2022; Masson-Delmotte et al., 2022), which is a key uncertainty for appropriate
91 climate mitigation and adaptation.

92 Moreover, evidence from warm intervals in the geological past suggests that the
93 subtropics may ultimately get wetter (rather than drier) under quasi-equilibrated warmer
94 conditions, i.e. “dry-gets-wetter”. For example, both the Miocene (23.0 to 5.3 million years
95 ago; Ma) and Pliocene (5.3 to 2.6 Ma) yield multi-proxy evidence for wetter subtropics in
96 southern Australia (Sniderman et al., 2016), North Africa (Hailemichael et al., 2002; Schuster
97 et al., 2009; Feng et al., 2022), South America (Carrapa et al., 2019), South-East Asia
98 (Wang et al., 2019; Feng et al., 2022), and western North American (Bhattacharya et al.,
99 2022). Burls and Federov (2017) suggest these wetter subtropical conditions were due to
100 weaker large-scale surface temperature gradients supporting weaker large-scale
101 atmospheric circulation and hence subtropical moisture divergence. Although the impact of
102 zonal-mean changes in circulation (dynamic effect) is often considered secondary to
103 changes in atmospheric humidity (thermodynamic effect), the former may be important
104 under certain climate scenarios (e.g., weak latitudinal temperature gradients; LTGs; see
105 also Byrne and O’Gorman, 2015) and may even compensate for an increase in
106 atmospheric humidity (Burls & Fedorov 2017). At a regional scale, enhanced monsoonal
107 circulation in the north Africa–east Asia region (Zhang et al., 2013; Feng et al., 2022)
108 and western North America (Bhattacharya et al., 2022) further account for the wetter climate
109 across those subtropical monsoon regions.

110 Here we focus on the early Eocene (56.0 to 47.8 million years ago; Ma) (Hollis et al.,
111 2019), an interval characterised by higher CO₂ values (> 1000 parts per million) (Anagnostou
112 et al., 2020), higher global mean surface temperature (10–16 °C warmer than pre-industrial)
113 (Inglis et al., 2020) and reduced pole-to-equator LTGs (of ~17 to 22°C) (Cramwinckel et al.,
114 2018; Evans et al., 2018; Gaskell et al., 2022). As such, this is an ideal interval to study how
115 changes in GMST and the LTG impact tropical, subtropical, mid- and high-latitude rainfall
116 patterns. However, there are very few quantitative early Eocene-aged MAP estimates,
117 particularly from the subtropics (15–30°N/S), and the hydrological response to warming
118 remains largely unknown. To resolve this, we utilise the recently published state-of-the-art
119 Deep-Time Model Intercomparison Project (DeepMIP) suite of Eocene model simulations
120 (Lunt et al., 2021) to explore the simulated global- and regional-scale hydrological response
121 to warming. This is combined with a new (terrestrial) proxy compilation to answer the
122 following questions: **i)** How does simulated tropical, subtropical, mid- and high-latitude MAP
123 and *P-E* respond to Eocene boundary conditions and increasing GMST, and what is the
124 level of agreement across the DeepMIP models? **ii)** What is the relative role of changes in
125 local evaporation versus moisture divergence (time-mean and eddy) in driving the MAP
126 changes? **iii)** Are early Eocene simulations characterised by a ‘wet-gets-wetter, dry-gets-
127 drier’ response? **iv)** How do the simulated thermodynamic (i.e., humidity) and dynamic (i.e.
128 circulation) effects contribute to changes in moisture transport in the subtropics? **v)** How well
129 do the DeepMIP models replicate proxy-derived MAP estimates?

130

131 **2 Methods**

132 **2.1 Modelling simulations**

133 *2.1.1 DeepMIP-Eocene simulations*

134 We make use of the DeepMIP suite of model simulations, embedded in the fourth phase of
135 the Paleoclimate Modelling Intercomparison Project (Kageyama et al, 2018), itself a part of
136 the sixth phase of the Coupled Model Intercomparison Project (CMIP6; (Eyring et al., 2016)).
137 An extensive description of the standard design of these model experiments is provided in

138 Lunt et al. (2017), and an overview of the large-scale climate features has been presented in
139 Lunt et al. (2021). The main advantage of these simulations over the EoMIP (Eocene
140 Modelling Intercomparison Project) “ensemble of opportunity” employed in earlier work
141 (Carmichael et al., 2016) is that the new DeepMIP simulations have been designed and
142 carried out using internally consistent Eocene boundary conditions (Herold et al., 2014; Lunt
143 et al., 2017). Simulations have been run at different atmospheric CO₂ levels – typically ×1,
144 ×3, ×6, and ×9 preindustrial (PI) CO₂, but with a subset of these, or additional atmospheric
145 CO₂ concentrations, chosen by some model groups (see Lunt et al., 2017; Lunt et al., 2021).
146 Different CO₂ experiments are expected to provide comparison targets to climate
147 reconstructions for different key time slices, including the early Eocene Climatic Optimum
148 (EECO; ~53.3–49.1 Ma), the Paleocene–Eocene Thermal Maximum (PETM; ~56 Ma), and
149 the latest Paleocene (i.e., pre-PETM). Pre-industrial simulations (×1 CO₂) with modern
150 continental configurations have also been performed to assess the influence of non-CO₂
151 Eocene boundary conditions. Simulations have been performed with eight different models
152 (**Table S1**) and detailed descriptions of the models and simulations are provided in Lunt et
153 al. (2021). To explore regional variations in hydroclimate, we subdivide our data into four
154 latitudinal bands: **I**) the tropics (0–15 °N/S), **II**) the subtropics (15–30 °N/S), **III**) the mid-
155 latitudes (30–60 °N/S), and **IV**) the high-latitudes (>60 °N/S). To further deconvolve the
156 cause of global and regional variations, we perform a moisture budget analysis. The
157 analysed climatologies are based on the last 100 years of each simulation. As different
158 models provided slightly different variables, for some models we were not able to provide
159 analysis of *P–E* (NorESM), or moisture budget analysis (IPSL, INMCM, and NorESM). We
160 compare observed changes in subtropical hydrology to changes in modelled latitudinal
161 temperature gradient (LTG), here taken as the difference in surface temperature between
162 the mid-latitudes (30–60 °N/S) and the tropics (15 °N–15 °S).

163

164 *2.1.2 Moisture Budget Analysis*

165 To diagnose the cause of $P-E$ changes within the DeepMIP ensemble, we conduct a
166 moisture budget analysis (Trenberth and Guillemot, 1995; Seager and Henderson, 2013).
167 This approach relies on the fact that climatological changes in $P-E$ – calculated over a long
168 enough timescale that fluctuations in the column integrated moisture content are negligible
169 (in our case the last 100 years of each DeepMIP simulation) – are balanced by the column-
170 integrated convergence of moisture in the overlying atmosphere, as follows:

$$P - E = -\nabla \cdot \frac{1}{g} \int_{p_t}^{p_s} \vec{v} q \, dp$$

171

172 where g is the acceleration due to gravity (ms^{-2}), q the atmospheric specific humidity (kg/kg),
173 and v the horizontal wind vector (ms^{-1}) integrated across pressure (p , Pa) levels from the
174 surface (p_s) to the top of the troposphere (tropopause; p_t). This climatological moisture
175 convergence can be further decomposed into its time-mean ($\overline{v} \overline{q}$) and eddy ($\overline{v' q'}$)
176 components. The time-mean component is calculated using the climatological mean data
177 provided in the DeepMIP dataset while the eddy component is calculated as the residual
178 between $P-E$ and the time-mean component given that the high temporal resolution data
179 required to calculate this term explicitly is not available as part of the DeepMIP dataset.

180

181 **2.2 Proxy synthesis**

182 *2.2.1 Approach*

183 Fossil leaves and palynomorphs (spores and pollen) can provide quantitative estimates of
184 MAP in the past. Using these, the primary approaches are: i) leaf physiognomy (i.e., leaf
185 shape) (Givnish, 1984; Wolfe, 1993; Wing and Greenwood, 1993; Greenwood, 2007) and ii)
186 nearest living relative (NLR)-based approaches (Pross et al., 2000; Greenwood et al., 2003;
187 Pancost et al., 2013; Suan et al., 2017; West et al., 2020). A multi-proxy approach combining
188 leaf physiognomy and NLR data is generally recommended and mitigates the different
189 uncertainties incorporated by individual approaches (e.g., West et al., 2020).

190 Methods based on leaf physiognomy utilise the correlation between the architecture
191 of leaves and climatic variables. As leaf size and shape are highly sensitive to moisture
192 availability (Givnish, 1984; Peppe et al., 2011; Spicer et al., 2021), fossil leaf architecture
193 can be related to precipitation using univariate methods such as Leaf Area Analysis (LAA)
194 (Wilf et al., 1998). The Climate Leaf Analysis Multivariate Program (CLAMP) (Wolfe, 1993,
195 1995) combines multiple leaf traits, including leaf area, leaf shape, and margin state (i.e.,
196 toothed or untoothed), to provide estimates of annual and seasonal precipitation (Spicer et
197 al., 2021). Anatomical characteristics of fossil wood can likewise reflect climate variables
198 (Wiemann et al., 1998; Poole and van Bergen, 2006). Although wood anatomy as a climate
199 proxy has not had widespread application in deep time climate compilations, multivariate
200 models of various wood anatomical characters are typically used (e.g., Poole et al., 2005).

201 Nearest living relative (NLR) approaches are based on the premise that the climatic
202 tolerance of a paleo-vegetation assemblage can be inferred from their presumed extant
203 relatives (e.g., Mosbrugger and Utescher, 1997; Fauquette et al., 1998; Greenwood et al.,
204 2003; Willard et al., 2019; West et al., 2020). These methods can be based on macrofossil
205 (most often leaf fossils but also seeds, fruits, or wood) or microfossil (i.e. sporomorphs)
206 paleobotanical assemblages, as long as the taxa can be correlated to a living relative with a
207 known climatic tolerance. The coexistence approach (CA; Mosbrugger and Utescher, 1997)
208 is a specific instance of this, in which the single climatic interval in which all NLRs can
209 coexist is reconstructed. More recent studies employing Bioclimatic Analysis (BA) typically
210 calculate probability density functions of climatic variables instead of minimum-to-maximum
211 intervals (e.g., Willard et al., 2019; West et al., 2020). The Climatic Amplitude Method (CAM)
212 is an alternative NLR approach that incorporates relative abundances of different taxa
213 (Fauquette et al., 1998).

214

215 *2.2.2 Proxy compilation*

216 Here we compile paleobotanical MAP estimates for the late Paleocene (59.2 to 56 Ma;
217 Thanetian) to early Eocene (56.0 to 47.8 Ma; Ypresian). Our compilation builds upon

218 previous EECO- (Carmichael et al., 2016) and Paleocene-Eocene Thermal Maximum
219 (PETM; 56 Ma)-aged (Carmichael et al., 2017) compilations. We supplement this with i)
220 published MAP estimates generated since, and ii) newly generated MAP estimates using
221 CLAMP and NLR on published palynological and macrofloral (predominantly leaf-based)
222 datasets. Our new proxy synthesis (n = 322) contains 133 MAP estimates (41%) from
223 Carmichael et al. (2016), 106 data points (33%) from other published sources, and 83 new
224 data points (26%) (**Figure 1; Table S1-2; Supplementary Data**). The new data in the
225 compilation helps to improve geographical coverage in previously data-poor regions,
226 including central west coast and eastern Africa (e.g., Eisawi and Schrank, 2008;
227 Adeonipekun et al., 2012; Cantrill et al., 2013) (also recently presented in Williams et al.,
228 2022); the coal and lignite bearing deposits of northeastern India and southern Pakistan
229 (Frederiksen, 1994; Tripathi et al., 2000; Verma et al., 2019); the Tibetan plateau and
230 sedimentary basins of southern China (e.g., Aleksandrova et al., 2015; Su et al., 2020; Xie et
231 al., 2020); and the South American (e.g., Quattrocchio and Volkheimer, 2000; Pardo-Trujillo
232 et al., 2003; Jaramillo et al., 2007) and North American continent and Caribbean islands
233 (e.g., Graham et al., 2000; Jarzen and Klug, 2010; Smith et al., 2020) (**Figure 1;**
234 **Supplementary Data**). Most of these use the NLR approach based on palynological
235 datasets, as plant macrofossils from the late Paleocene – early Eocene low latitudes are
236 more rarely preserved, although some exceptions are known (Wing et al., 2009; Shukla et
237 al., 2014; Herman et al., 2017). We also incorporate data from the mid and high latitudes,
238 e.g., southern South America, North America, Australia and New Zealand, and high Siberia
239 (**Supplementary Data**). For regions with exceptionally poor data coverage (e.g., tropical and
240 subtropical latitudes, Antarctica), we also compile and generate MAP estimates from the
241 early middle Eocene (47.8 to ~45 Ma; first half of the Lutetian). Published CLAMP and NLR
242 data were re-analysed following recent recommendations, so that there is no bias as a result
243 of discrepant methodology. Specifically, 1) CLAMP-scored fossil leaf assemblages were re-
244 analysed using up-to-date geographically appropriate calibration datasets (Kennedy et al.,
245 2014; Yang et al., 2015; Reichgelt et al., 2019), 2) for both CLAMP and NLR reconstructions,

246 gridded climate datasets from the R package *dismo* were employed (Hijmans et al., 2020),
247 and 3) NLR analysis was performed using consistently filtered modern distribution datasets
248 to avoid regional overrepresentation (e.g. West et al., 2020). Modern site coordinates and
249 age constraints were extracted from the original publications.

250

251 2.2.3 *Data-model comparison framework*

252 To compare proxy and model data, we employ a data comparison similar to that used for the
253 Miocene MioMIP ensemble (Burls et al., 2021). This approach requires inclusion of
254 uncertainty for both the proxy and model MAP estimates. To account for site location
255 uncertainty, we determine site co-ordinates for the age range of our proxy data compilation
256 above, i.e., from 59 Ma (late Paleocene) to 45 Ma (early middle Eocene) using the Müller et
257 al. (2016) Gplates continental polygons in combination with the hotspot-based rotation frame
258 of Matthews et al. (2016) (i.e., analogous to all DeepMIP simulations apart from NorESM;
259 Lunt et al., 2020). For the model simulations, MAP values are taken from the grid cells that
260 fall within the proxy location uncertainty. The model MAP uncertainty is subsequently defined
261 as the range between minimum and maximum MAP within these model grid cells. For proxy
262 estimates, we use the proxy error and error type as reported in the original study. Typically,
263 this is a minimum–maximum range or confidence interval (e.g., 95%) for NLR approaches
264 (e.g., Willard et al., 2019; West et al., 2020), and standard error (SE) or standard deviation
265 (SD) derived from calibration dataset residuals for leaf physiognomy methods (e.g.,
266 Teodoridis et al., 2011). For our newly generated values, uncertainties are reported as 95%
267 confidence interval for NLR and ± 1 SD for CLAMP. The subsequent overlap between the
268 model and proxy uncertainty range is assessed following the MioMIP methodology (Burls et
269 al., 2021). Any overlap between the proxy and model uncertainty ranges is defined as “no
270 bias” (Figure S1 in Burls et al., 2021).

271

272 **3 Results and Discussion**

273 **3.1 DeepMIP models reproduce pre-industrial global precipitation patterns**

274 Each model included in the DeepMIP suite is able to reproduce the main features of pre-
275 industrial precipitation patterns (**Figure 2, Figure S1**). However, some common model
276 precipitation biases are apparent. For example, all simulations exhibit a double Inter-Tropical
277 Convergence Zone (ITCZ) in MAP, simulating excess precipitation south of the equator. This
278 bias is common and the double ICTZ remains a consistent error in both the previous (e.g.,
279 CMIP3, CMIP5) and latest (CMIP6) generation of climate models (Tian & Dong 2020). There
280 is also a lack of simulated precipitation in the western equatorial Pacific (**Figure 2c**). Never-
281 the-less, the shape of the South Pacific convergence zone (SPCZ) is improved in the multi-
282 model mean (MMM) compared to the previous EoMIP generation model simulations
283 (Carmichael et al., 2016).

284

285 **3.2 Influence of non-CO₂ boundary conditions on the early Eocene hydrological** 286 **cycle**

287 Non-CO₂ boundary conditions (i.e., paleogeography, vegetation, aerosols) can exert an
288 influence on global and regional MAP and *P-E* values. The previous EoMIP ensemble found
289 a minor role for non-CO₂ boundary conditions on global MAP (+0.1 mm/day; Carmichael et
290 al., 2016). However, this was only performed for a single model simulation (HadCM3L). To
291 better isolate the influence of non-CO₂ boundary conditions on the early Eocene hydrological
292 cycle, we compared early Eocene 1x CO₂ simulations and pre-industrial 1x CO₂ simulations
293 from multiple (n=6) DeepMIP models.

294 At a global scale, the early Eocene 1x CO₂ simulations are characterised by higher
295 MAP values relative to pre-industrial (0.1 to 0.4 mm/day; 1x CO₂ symbols in **Figure 3**). This
296 is because the early Eocene 1xCO₂ simulations have higher global mean surface
297 temperatures (~3–5°C) relative to the preindustrial 1x CO₂ control simulations (see also Lunt
298 et al., 2021) (**Figure S2**). This leads to enhanced surface evaporation which is balanced by
299 precipitation globally (Held and Soden, 2006; Siler et al., 2019).

300 At a regional scale, the early Eocene 1x CO₂ simulations are characterised by higher
301 MAP estimates in the tropics (0-15° N/S), mid-latitudes (30-60 °N/S), and high-latitudes (>60

302 °N/S) (typically +0.1 to +0.4 mm/day, but up to +0.6 mm/day in the high-latitudes, **Figure 4**
303 and **5; Figure S3**) relative to pre-industrial. The tropics, mid-latitudes, and high-latitudes are
304 also characterised by positive $P-E$ values (typically +0.1 to 0.2 mm/day, but up to +0.4
305 mm/day in the high-latitudes; **Figure 4** and **6; Figure S4** and **S5**) relative to pre-industrial.
306 Furthermore, the tropics are characterised by an eastward shift and expansion in deep
307 tropical convection, and hence the Walker Circulation, over the Pacific Ocean (**Figure 4**).
308 Focusing on the ITCZ, non-CO₂ Eocene boundary condition only affect the width of the ITCZ
309 (defined as in Byrne and Schneider, 2016) in CESM and MIROC, where it increases slightly
310 (**Figure 7a**). Additionally, the ITCZ latitude of maximum precipitation shifts northwards
311 relative to the preindustrial control in 3 (CESM, HadCM3B and MIROC) of the 5 models that
312 did the 1xCO₂ experiment (**Figure 7b**). The subtropical (15–30 °N/S) early Eocene 1x CO₂
313 MMM difference from the pre-industrial is characterised by negative $P-E$ values (-0.2 to -0.8
314 mm/day; **Figure 6; Figure S4** and **S5**), but the associated MAP estimates span a wide
315 range and can be higher (i.e., CESM, GFDL, MIROC; 0.1 to 0.6 mm/day) or lower (i.e.,
316 COSMOS, HadCM3L, HadCM3LB; -0.1 to -0.2 mm/day) relative to pre-industrial (**Figure 5;**
317 **Figure S3**). When assessing the relative roles of local evaporation, time-mean moisture
318 transport divergence, and eddy moisture transport divergence changes, generally the
319 models with increased 1x CO₂ subtropical MAP (i.e., CESM, GFDL, MIROC) experience
320 increased local subtropical evaporation that is not completely counteracted by the enhanced
321 time-mean moisture divergence (**Figure 8c, Figure S6b**).

322

323 **3.3 Global and zonal-mean variability in the early Eocene hydrological cycle**

324 The DeepMIP simulations span a wide range of CO₂ concentrations (x1 to x9 PI CO₂) and
325 GMST (~17 to 35°C) and can thus provide insights into the global- and regional-scale
326 hydrological response to CO₂-induced warming. Across the DeepMIP ensemble, higher
327 GMST estimates are associated with higher global-mean MAP estimates as warming leads
328 to enhanced surface evaporation, both between different models and within the same model
329 at different CO₂ levels (**Figure 3**). Similar to previous studies (e.g. Held and Soden 2006;

330 Siler et al., 2019) and the latest CMIP models (MMM = 2.51%/K with a range of 2.1 – 3.1%/K
331 per Pendergrass, 2020) the best linear fit across the entire DeepMIP ensemble is a 2.4%
332 increase in global MAP per degree of warming.

333 Next to this global perspective, there are also zonal-mean variations in MAP that
334 differ in their relationship with GMST (**Figure 5**). In the tropics (0–15 °N/S), the mid-latitudes
335 (30–60 °N/S) and the high-latitudes (>60 °N/S), higher GMST estimates are associated with
336 higher MAP estimates, with the greatest sensitivity to GMST in the high latitudes (9.1%
337 increase in precipitation per °C warming; **Figure 5d**). As CO₂ and hence GMST increases,
338 both enhanced local evaporation and time-mean moisture convergence are responsible for
339 the rise in tropical precipitation across the DeepMIP multi-model ensemble (**Figure S6a**).
340 The width of the ITCZ decreases with increased CO₂ in 5 (CESM, COSMOS, HadCM3B,
341 HadCM3BL and MIROC) of the 6 models that provided the meridional wind field variable
342 required to perform ITCZ width calculations (**Figure 7a**). This is consistent with recent data-
343 assimilation based work focusing on the PETM (Tierney et al, 2022). To varying degrees, the
344 ITCZ latitude of maximum precipitation shifts southwards with increasing CO₂ in most of the
345 models (**Figure 7b**). Turning to the high-latitudes, increased local evaporation and time-
346 mean plus eddy moisture convergence work together to maintain the greatest sensitivity of
347 MAP to GMST in the high latitudes (**Figure S6d**). Similar to the tropics and high-latitudes,
348 increased local evaporation with elevated CO₂ concentrations plays a key role in increasing
349 mid-latitude MAP values. However, much like the subtropics discussed next, there are
350 significant model differences in the (relatively minor) contribution of the time-mean and eddy
351 moisture flux divergence terms (**Figure S6c**).

352 In the subtropics (15–30 °N/S), the relationship between GMST and MAP differs
353 greatly between the DeepMIP model simulations. For this latitudinal band there is a wide
354 range in MAP estimates: HadCM3, MIROC and COSMOS simulate lower MAP values
355 relative to pre-industrial, whereas CESM and GFDL simulate higher MAP values relative to
356 pre-industrial (**Figure 5b**). Moisture budget diagnostics (see below) suggest that a weaker

357 latitudinal temperature gradient is the cause of higher subtropical MAP values in both CESM
 358 and GFDL.

359 For a given global mean temperature change, the DeepMIP models also exhibit
 360 different zonal-mean $P-E$ responses. In the tropics and the high-latitudes, higher GMST
 361 estimates are associated with more positive $P-E$ values and overall wetter conditions
 362 (**Figure 6**). In the subtropics, higher GMST estimates are associated with more negative $P-E$
 363 values and overall drier conditions (**Figure 6b**). This indicates that from a zonal-mean
 364 perspective the early Eocene largely conforms to the ‘wet-gets-wetter, dry-gets-drier’
 365 hypothesis within the DeepMIP simulations. Lastly, there is a weak relationship between
 366 GMST and $P-E$ values in the mid-latitudes (**Figure 6c**). As the mid-latitude band
 367 encompasses both positive and negative $P-E$ values compared to pre-industrial (ca. -2 to +2
 368 mm/day; **Figure 4**), the lack of relationship between CO_2 and temperature in this zonally-
 369 averaged view is perhaps unsurprising.

370 Our moisture budget analysis (**Figure 8; Figure S8**) lends further insight into the
 371 mechanisms driving the simulated subtropical $P-E$ changes. Generally speaking, the time-
 372 mean component is the dominant component in the tropics, where the time mean moisture
 373 transport typically dominates over the eddy component (**Figure 8c-8d**). Changes in net $P-E$
 374 values ($\delta(P-E)$) due to the time mean component can be further decomposed into: i)
 375 changes in humidity assuming constant preindustrial circulation ($\bar{v}_{cnt} \delta \bar{q}$, the thermodynamic
 376 component of changes in the time mean moisture divergence), ii) changes in circulation
 377 assuming constant preindustrial humidity ($\delta \bar{v} \bar{q}_{cnt}$, the dynamic component of changes in the
 378 time mean moisture divergence), and iii) a perturbation term representing the coupling of
 379 changes in humidity and changes in circulation ($\delta \bar{v} \delta \bar{q}$) (**Figures 8e-f; Figure S9**):

380

$$\delta(P - E)_{tm} = -\nabla \cdot \frac{1}{g} \int_{p_t}^{p_s} v_{cnt} \delta q \, dp - \nabla \cdot \frac{1}{g} \int_{p_t}^{p_s} \delta v q_{cnt} \, dp - \nabla \cdot \frac{1}{g} \int_{p_t}^{p_s} \delta v \delta q \, dp + RES$$

381

382 where “tm” indicates time mean, δ represents the change in each variable between the study
383 interval (i.e., the early Eocene) and the pre-industrial climate, and the residual term (RES)
384 accounts for changes in the surface pressure bound of the integrals, which is dominated by
385 topographic changes between the Eocene and pre-industrial experiments. With increasing
386 temperatures, atmospheric humidity (q) is predicted to increase following the Clausius-
387 Clapeyron relation. Assuming that the zonal-mean circulation (v) remains identical to pre-
388 industrial ($\delta v = 0$), the dynamic term will be zero and the thermodynamic term will result in
389 the tropics and high-latitudes becoming wetter (i.e. the moisture convergence into these
390 regions in the control climate is enhanced) and the subtropics becoming drier (i.e., the
391 moisture divergence from this region in the control climate is enhanced). Zonal-mean
392 circulation changes are often considered secondary to changes in atmospheric humidity.
393 However, it has been demonstrated that zonal-mean circulation changes may be
394 important under certain climate scenarios (e.g., weak latitudinal temperature gradients)
395 and may even compensate for changes in atmospheric humidity in regions such as the
396 subtropics on zonal average (Burls & Fedorov 2017). In a scenario where zonal-mean
397 circulation (v) – specifically a decrease in Hadley cell strength – dominates over an
398 increase in humidity (q), the subtropics on average will be characterised by reduced
399 (rather than enhanced) moisture divergence and wetter (rather than drier) conditions
400 (Burls & Fedorov 2017).

401 Focusing on the subtropics in the DeepMIP simulations (**Figure 9**), higher GMST
402 values indeed result in an increase in atmospheric humidity and enhanced subtropical
403 moisture divergence. This leads to a corresponding decrease in $P-E$ (up to > -1.5 mm/day;
404 **Figure 9a**) and is consistent with a ‘wet-gets-wetter, dry-gets-drier’ scenario in warmer
405 climates. However, this scenario is partially compensated by a reduction in LTGs, here taken
406 as the difference between $15^{\circ}\text{S}-15^{\circ}\text{N}$ and $30-60^{\circ}\text{N/S}$. Reduced LTGs lead to a reduction in
407 the strength of the zonal-mean subtropical circulation (v) – i.e., the Hadley circulation – and
408 a relative increase in subtropical zonal-mean $P-E$ (**Figure 9b**), particularly in the Southern
409 Hemisphere where the strength of the Hadley Cell (**Figure S10**) systematically weakens with

410 the LTG in all models (**Figure S12b & 11e**). The models differ more in the strength of the
411 relationship between Hadley circulation changes and the LTG in the Northern Hemisphere
412 (**Figure S12d & S12f**), perhaps because of the complicating factor of inter-model differences
413 in latitudinal ITCZ shift. The dynamical effect of weakened Hadley circulation is stronger in
414 model simulations with weaker latitudinal temperature gradients (i.e., CESM and GFDL
415 model simulations) and weaker in models with stronger latitudinal temperature gradients
416 (e.g., HadCM3L) (**Figure 9d & S12b**). Therefore, the DeepMIP models with the lowest LTGs
417 (e.g., CESM and GFDL) are characterized by higher subtropical MAP estimates relative to
418 pre-industrial. Intriguingly, those models with reduced LTGs most closely reproduce
419 temperature gradients (and GMST estimates) as reconstructed by proxies (Zhu et al., 2019;
420 Figure 1 in Lunt et al., 2021). This implies that the early Eocene was likely characterized by
421 a reduction in the strength of Hadley circulation. However, all DeepMIP models, including
422 CESM and GFDL, show that the reduction in subtropical circulation (**Figure 9d**) is not
423 sufficient to compensate fully for changes in atmospheric humidity (**Figure 9c**). As such, the
424 subtropics are characterised by overall drier conditions in terms of $P-E$ in the DeepMIP
425 ensemble (**Figure 9a**).

426 Extrapolating from this, if early Eocene LTGs were even weaker than suggested by
427 these models (Lunt et al., 2021), Hadley circulation-induced changes may have
428 outcompeted the thermodynamic changes, leading to overall wetter subtropics on zonal
429 average (e.g. Burls & Federov, 2017). Although proxy-model bias has decreased over recent
430 years for certain DeepMIP models, overall, early Eocene proxy compilations still suggest
431 weaker global equator-to-pole LTGs (~14 to 22°C; Gaskell et al., 2022; Evans et al., 2018;
432 Cramwinckel et al., 2018) than those predicted in the DeepMIP model ensemble (~18 to
433 25°C; Figure 1b in Lunt et al., 2021). However, proxy-derived LTG estimates remain
434 associated with large uncertainties due to proxy-inherent uncertainties, the use of different
435 input datasets, and/or the analysis of different time intervals (*cf.* GMST estimates; Inglis et
436 al., 2020). Taken together, this highlights the important role of accurately reconstructing

437 and modelling the meridional temperature gradient when interpreting past meridional
438 rainfall patterns.

439

440 **3.4 Proxy-based precipitation estimates during the early Eocene**

441 Our proxy synthesis indicates that high-latitude regions were characterised by high MAP
442 estimates, consistent with previous results from the northern (Eberle and Greenwood, 2012;
443 West et al., 2015; Suan et al., 2017; Salpin et al., 2019; West et al., 2020) and southern
444 high-latitudes (Poole et al., 2005; Pross et al., 2012) (**Figure 10**). This is consistent with
445 evidence for low-salinity sea surface conditions in the high northern latitudes near the
446 termination of the EECO (~49 Ma) (i.e., the Azolla interval), although this salinity signal
447 might be strongly linked to paleogeographic change (Brinkhuis et al., 2006; Barke et al.,
448 2012). Proxy estimates from more transient periods of warming (e.g., the PETM and Eocene
449 Thermal Maximum 2; ETM2) provide additional support for high MAP in the Arctic (Pagani et
450 al., 2006; Willard et al., 2019), the North Sea Basin (Kender et al., 2012; Garel et al., 2013;
451 Collinson et al., 2003), and the southwest Pacific (Sluijs et al., 2011; Pancost et al., 2013).
452 We note that in our compilation, early Eocene-aged CLAMP-derived MAP estimates from
453 North America are much higher than most NLR estimates. CLAMP estimates are based on
454 locally derived floral assemblages, whereas NLR estimates can reflect both locally derived
455 floral elements but also floral elements transported over long distance (e.g. wind- or water-
456 dispersed pollen). As a consequence, CLAMP estimates may reflect a bias towards wetter
457 environments, whereas NLR estimates may be biased towards drier (upland) environments.
458 The set of MAP estimates from Antarctica based on wood physiognomy are also far higher
459 than the other proxies (Poole et al., 2005). Due to the lack of wood physiognomic MAP
460 estimates from other regions, it is unclear whether these values are representative of the
461 Antarctic continent.

462 Early Eocene tropical and subtropical MAP estimates are also relatively high (> 2 to 4
463 mm/day, **Figure 10**). Although proxy-derived subtropical MAP values imply wetter conditions
464 during the early Eocene, we note that these estimates are biased towards regions with well-

465 preserved floral assemblages and, by extension, relatively wet regions. Subsequently, arid
466 and semi-arid environments are likely under-sampled in our synthesis. Evidence from
467 periods of superimposed warming during the Eocene suggests drier subtropics, with
468 evidence for enhanced evapotranspiration in Tanzania during the onset of the PETM
469 (Handley et al., 2012), drying in the continental interior (e.g., Bighorn Basin) during the body
470 of the PETM (Smith et al., 2007; Kraus and Riggins, 2007; Kraus et al., 2013), and increased
471 subtropical salinity in the central Pacific during ETM2 (Harper et al., 2017). Based on the
472 sparsity of data for the early Eocene background state however, we cannot distinguish
473 whether the lack of paleobotanical evidence for arid environments derives from sampling
474 sparsity itself, from methodological bias, or from actual absence of such environments.
475 Moving forward, we suggest that alternative proxies, for example clumped isotope- $\delta^{18}\text{O}$
476 analysis of pedogenic siderites (van Dijk et al., 2020), could help to reconstruct hydrological
477 change in arid and semi-arid environments where plant macrofossils are unlikely to be
478 preserved, and the availability of plant-based terrestrial proxy data will therefore be limited or
479 absent. These caveats will need to be addressed in the future to fully establish the fidelity
480 with which the DeepMIP-Eocene models simulate the tropical and subtropical hydrological
481 cycle response over land. In this study, we proceed by evaluating the models with our
482 synthesis of paleobotanical MAP estimates.

483

484 **3.5 Terrestrial precipitation data-model comparison**

485 To explore whether the DeepMIP models realistically reproduce regional MAP patterns
486 during the early Eocene, we employ the data-model comparison approach outlined in
487 Section 2.2.3 using our new and published botanical-based MAP estimates. Although the
488 ‘wet-gets-wetter, dry-gets-drier’ response may not hold true over land (Byrne and O’Gorman,
489 2015), our terrestrial data-model comparison helps us assess overall model performance. A
490 previous site-by-site data-model comparison (Carmichael et al., 2016) suggested that the
491 EoMIP models were able to reproduce key features of the hydrological cycle in the mid-
492 latitudes (e.g., western US interior, central Europe), but modelled MAP estimates were

493 typically lower than those from proxies in the high-latitudes (e.g., East Antarctica, SE
494 Australia, Axel Heiberg). For the new DeepMIP-Eocene model-data comparison, we find a
495 similar result (**Figure 11 & 12**). The MMM underestimates proxy-derived MAP in the high
496 northern latitudes, especially at lower CO₂ levels (**Figure 11**). We attribute this mismatch to
497 the lack of polar amplification in certain models, especially at lower CO₂ levels (e.g.,
498 HadCM3, COSMOS) (Lunt et al., 2021, **Figure S11**). At high CO₂ values, the model-data
499 bias for high-latitude MAP is smallest, down to -0.4 to -0.6 mm/day for the 6x and 9x CO₂
500 simulations (**Figure 12d**). The mid latitudes are likewise associated with large data-model
501 mismatches, with models simulating MAP values that are too low by ~0.4 to 1.3 mm/day
502 from a zonal-mean perspective, and a decrease in bias with increasing CO₂ levels (**Figure**
503 **12c**). Moving to the subtropics, model-bias is likewise negative, with a large range between
504 near-zero and -1.75, but without a clear intra- or inter-model improvement with CO₂ levels.
505 Finally, almost all models (except for COSMOS) simulate too much precipitation in the
506 tropics compared to the reconstructions, with positive biases of up to +1.5 mm/day, that
507 remain similar or worsen with increasing CO₂ for a given model (**Figure 12a**).

508

509 Comparing between models, proxy-model mismatches are lowest for CESM, GFDL, MIROC
510 and NorESM in the subtropics, mid- and high latitudes (**Figure 12; Figure S11**) i.e., the
511 models with higher GMST estimates and lower LTGs (Lunt et al., 2021). These models
512 overall simulate higher precipitation. They however do not outperform the other models in
513 the tropical band (**Figure 12a**). From a regional viewpoint, in the mid-latitudes the MMM
514 either underestimates MAP (e.g., western South America and Tibet) or overestimates MAP
515 (e.g., western North America; **Figure 11**). As these mismatches lie close to major mountain
516 ranges (e.g., Rocky Mountains, proto-Tibetan Plateau, Andes), it is possible that mismatches
517 are due to topographic effects as a small offset in reconstructed paleolocation can make a
518 large difference in reconstructed elevation. Additionally, the DeepMIP Eocene model
519 resolution is coarse and the topography has inherent uncertainty, especially in the North
520 American Cordillera and proto-Himalayas (Herold et al. 2014). In our MMM comparison, it

521 should be noted that the composition of the model ensemble changes over the different CO₂
522 levels in the MMM (cf. **Table S1** and **Figure 4**). For instance, whereas the 3xCO₂
523 experiment was performed with 7 out of 8 DeepMIP models, only 3 models (CESM, GFDL,
524 INMCM) were used for the 6xCO₂ experiment, and only CESM ran a 9xCO₂ simulation. For
525 a more detailed analysis of regional hydroclimate in the DeepMIP simulations, we refer the
526 reader to Williams et al. (2022) and Reichgelt et al. (2022), for the African and Australian
527 continent, respectively.

528

529 Our results indicate that the models with higher GMST and weaker LTGs are able to better
530 simulate the global and regional scale hydrological cycle (**Figure 12**). Overall, our integrated
531 data-model approach suggests that the early Eocene was characterised by a
532 thermodynamically-dominated hydrological response to warming within the mid and high
533 latitudes. Enhanced polar amplified warming in response to increased CO₂ forcing leads to
534 an improved high-latitude model-proxy fit with enhanced local evaporation and eddy
535 moisture transport convergence increasing precipitation (**Figure S6; Figure 12c-d; Figure**
536 **S11**). Furthermore, the DeepMIP-Eocene models on average simulate higher precipitation in
537 the tropics relative to the proxy data (**Figure 12a; Figure S11**), with increased tropical
538 precipitation driven by enhanced local evaporation and time-mean moisture convergence.
539 While several DeepMIP-Eocene models simulate a narrowing of the ITCZ, an ITCZ
540 narrowing signal is not clearly evident within the proxy data (**Figure 10**). Lastly, in the
541 subtropical latitudes, the models differ widely in their response leading to varying degrees of
542 model-data bias (**Figure 12b**). Weakened Hadley circulation in response to weaker LTGs
543 could have offset thermodynamic subtropical drying and supported regional wetting, as seen
544 to some extent in the GFDL and CESM models (**Figure 12b; Figure S10**). Although the lack
545 of proxy evidence for arid subtropical regions in the early Eocene background state might be
546 caused by a bias of the sparsely available data to wet regions, this conspicuous absence of
547 evidence at least reflects regionally wetter conditions.

548

549 **4 Conclusions**

550 Here we use the DeepMIP model simulations to investigate global and zonal-mean rainfall
551 patterns during the early Eocene (~56.0–47.8 million years ago). Across the DeepMIP
552 ensemble, higher GMST estimates are associated with higher global-mean MAP estimates,
553 with an overall 2.4% increase in global MAP per degree of warming. At higher temperatures,
554 the DeepMIP model simulations indicate that - on average - the low- (0-15° N/S) and high-
555 latitudes (>60° N/S) are characterised by positive $P-E$ values (wetter conditions). While the
556 subtropics (15-30° N/S) are characterised by negative $P-E$ values (drier conditions), there is
557 large inter-model variability in subtropical mean annual precipitation (MAP) due to the
558 competing influence of humidity (i.e., thermodynamic changes) and atmospheric
559 circulation (i.e., dynamic changes) in this region. The DeepMIP model simulations that
560 exhibit higher subtropical MAP estimates relative to pre-industrial are characterised by
561 weaker latitudinal temperature gradients and a reduction in subtropical moisture divergence.
562 This acts to offset drier conditions, particularly in the Southern Hemisphere where the
563 strength of the Hadley Cell systematically weakens with the latitudinal temperature gradient
564 in all models. Crucially, the models with reduced latitudinal temperature gradients (e.g.,
565 GFDL, CESM) more closely reproduce our compilation of proxy-derived precipitation
566 estimates and other key climate metrics. Taken together, this implies weaker subtropical
567 circulation in the early Eocene. However, changes in subtropical moisture divergence were
568 not sufficient to induce subtropical wetting in the models. Extrapolating from this, if early
569 Eocene latitudinal temperature gradients were even weaker than suggested by these
570 models, circulation-induced changes may have outcompeted the thermodynamic changes,
571 leading to overall wetter subtropics – consistent with sparsely available proxy data. Taken
572 together, our study highlights the importance of accurately reconstructing and modelling
573 the meridional temperature gradient when interpreting past subtropical rainfall patterns.

574

575 **Open Research**

576 The paleobotanical data used to calculate mean annual precipitation (MAP) estimates is
577 available at OSF (<https://doi.org/10.17605/OSF.IO/M7B4K>) and associated with a CC-BY 4.0
578 license (Cramwinckel et al., 2023). Version 1.0.0 of the DeepMIP-Eocene model database
579 used to simulate Eocene climate is preserved online (<https://www.deepmip.org/data-eocene>)
580 and openly available via the University of Bristol Research Data Storage Facility (RDSF)
581 (Lunt, 2023).

582

583

584 **Acknowledgments**

585 G.N.I and M.J.C. were supported by a Royal Society Dorothy Hodgkin Fellowship
586 (DHF1R1\191178). G.N.I. was also supported by additional funds from the Royal Society
587 (DHF1ERE\210068). N.J.B. was supported by the National Science Foundation, via award
588 AGS-1844380. D.G was supported by the Natural Sciences and Engineering Research
589 Council of Canada (NSERC) through Discovery Grants (DG 311934 and 2016-04337).
590 C.K.W acknowledges funding from a private donor to the Northern Climates Postdoctoral
591 Fellowship at the University of Alberta. D.K.H acknowledges support from Australian
592 Research Council grant DE22010079 and the Australian Centre for Excellence in Antarctic
593 Science, project number SR200100008. R.F is supported by NSF-2114204. A.dB was
594 supported by Swedish Research Council project 2020-04791. The GFDL simulations were
595 performed by resources provided by the Swedish National Infrastructure for Computing
596 (SNIC) at the National Supercomputer Centre (NSC), partially funded by the Swedish
597 Research Council through grant agreement no. 2018-05973. W.L.C and A.A.O acknowledge
598 funding from JSPS KAKENHI (Grant no. 17H06104) and MEXT KAKENHI (Grant no.
599 17H06323). The CESM project is supported primarily by the National Science Foundation
600 (NSF); this material is based upon work supported by the National Center for Atmospheric
601 Research, which is a major facility sponsored by the NSF under Cooperative Agreement No.
602 1852977.

603

604 **Conflict of Interest**

605 The authors declare no conflicts of interest relevant to this study.

606

607 **Reference list**

608 Adeonipekun, P. A., Ehinola, O. A., Toluhi, Yussuph, I. A., Toluhi, A., and Oyelami, A.: Bio-
609 Sequence Stratigraphy of Shagamu Quarry Outcrop, Benin Basin, Southwestern Nigeria, 2012.

610 Aleksandrova, G. N., Kodrul, T. M., and Jin, J. H.: Palynological and paleobotanical
611 investigations of Paleogene sections in the Maoming basin, South China, *Stratigr. Geol. Correl.*,
612 23, 300–325, <https://doi.org/10.1134/S0869593815030028>, 2015.

613 Anagnostou, E., John, E. H., Babila, T. L., Sexton, P. F., Ridgwell, A., Lunt, D. J., Pearson, P. N.,
614 Chalk, T. B., Pancost, R. D., and Foster, G. L.: Proxy evidence for state-dependence of climate
615 sensitivity in the Eocene greenhouse, *Nat. Commun.*, 11, 4436, [https://doi.org/10.1038/s41467-](https://doi.org/10.1038/s41467-020-17887-x)
616 020-17887-x, 2020.

617 Barke, J., van der Burgh, J., van Konijnenburg-van Cittert, J. H. A., Collinson, M. E., Pearce, M.
618 A., Bujak, J., Heilmann-Clausen, C., Speelman, E. N., van Kempen, M. M. L., Reichart, G.-J.,
619 Lotter, A. F., and Brinkhuis, H.: Coeval Eocene blooms of the freshwater fern *Azolla* in and
620 around Arctic and Nordic seas, *Palaeogeogr. Palaeoclimatol. Palaeoecol.*, 337–338, 108–119,
621 <https://doi.org/10.1016/j.palaeo.2012.04.002>, 2012.

622 Bhattacharya, T., Feng, R., Tierney, J. E., Rubbelke, C., Burls, N., Knapp, S., and Fu, M.:
623 Expansion and Intensification of the North American Monsoon During the Pliocene, *AGU Adv.*, 3,
624 e2022AV000757, <https://doi.org/10.1029/2022AV000757>, 2022.

625 Brinkhuis, H., Schouten, S., Collinson, M. E., Sluijs, A., Damsté, J. S. S., Dickens, G. R., Huber,
626 M., Cronin, T. M., Onodera, J., Takahashi, K., Bujak, J. P., Stein, R., van der Burgh, J., Eldrett, J.
627 S., Harding, I. C., Lotter, A. F., Sangiorgi, F., Cittert, H. van K., de Leeuw, J. W., Matthiessen, J.,

- 628 Backman, J., Moran, K., and the Expedition 302 Scientists: Episodic fresh surface waters in the
629 Eocene Arctic Ocean, *Nature*, 441, 606–609, <https://doi.org/10.1038/nature04692>, 2006.
- 630 Burls, N. J., Bradshaw, C. D., Boer, A. M. D., Herold, N., Huber, M., Pound, M., Donnadiou, Y.,
631 Farnsworth, A., Frigola, A., Gasson, E., Heydt, A. S. von der, Hutchinson, D. K., Knorr, G.,
632 Lawrence, K. T., Lear, C. H., Li, X., Lohmann, G., Lunt, D. J., Marzocchi, A., Prange, M.,
633 Riihimaki, C. A., Sarr, A.-C., Siler, N., and Zhang, Z.: Simulating Miocene Warmth: Insights From
634 an Opportunistic Multi-Model Ensemble (MioMIP1), *Paleoceanogr. Paleoclimatology*, 36,
635 e2020PA004054, <https://doi.org/10.1029/2020PA004054>, 2021.
- 636 Byrne, M. P. and O’Gorman, P. A.: The Response of Precipitation Minus Evapotranspiration to
637 Climate Warming: Why the “Wet-Get-Wetter, Dry-Get-Drier” Scaling Does Not Hold over Land, *J.*
638 *Clim.*, 28, 8078–8092, <https://doi.org/10.1175/JCLI-D-15-0369.1>, 2015.
- 639 Byrne, M. P. and Schneider, T.: Energetic Constraints on the Width of the Intertropical
640 Convergence Zone, *J. Clim.*, 29, 4709–4721, <https://doi.org/10.1175/JCLI-D-15-0767.1>, 2016.
- 641 Cantrill, D. J., Bamford, M. K., Wagstaff, B. E., and Sauquet, H.: Early Eocene fossil plants from
642 the Mwadui kimberlite pipe, Tanzania, *Rev. Palaeobot. Palynol.*, 196, 19–35,
643 <https://doi.org/10.1016/j.revpalbo.2013.04.002>, 2013.
- 644 Carmichael, M. J., Lunt, D. J., Huber, M., Heinemann, M., Kiehl, J., LeGrande, A., Loptson, C. A.,
645 Roberts, C. D., Sagoo, N., Shields, C., Valdes, P. J., Winguth, A., Winguth, C., and Pancost, R.
646 D.: A model–model and data–model comparison for the early Eocene hydrological cycle, *Clim*
647 *Past*, 12, 455–481, <https://doi.org/10.5194/cp-12-455-2016>, 2016.
- 648 Carmichael, M. J., Inglis, G. N., Badger, M. P. S., Naafs, B. D. A., Behrooz, L., Rimmelzwaal, S.,
649 Monteiro, F. M., Rohrssen, M., Farnsworth, A., Buss, H. L., Dickson, A. J., Valdes, P. J., Lunt, D.
650 J., and Pancost, R. D.: Hydrological and associated biogeochemical consequences of rapid
651 global warming during the Paleocene-Eocene Thermal Maximum, *Glob. Planet. Change*, 157,
652 114–138, <https://doi.org/10.1016/j.gloplacha.2017.07.014>, 2017.

- 653 Carrapa, B., Clementz, M., and Feng, R.: Ecological and hydroclimate responses to
654 strengthening of the Hadley circulation in South America during the Late Miocene cooling, *Proc.*
655 *Natl. Acad. Sci.*, 116, 9747–9752, <https://doi.org/10.1073/pnas.1810721116>, 2019.
- 656 Collinson, M. E., Hooker, J. J., and Groecke, D. R.: Cobham lignite bed and
657 penecontemporaneous macrofloras of southern England: A record of vegetation and fire across
658 the Paleocene-Eocene Thermal Maximum, <https://doi.org/10.1130/0-8137-2369-8.333>, 2003.
- 659 Cramwinckel, M. J., Huber, M., Kocken, I. J., Agnini, C., Bijl, P. K., Bohaty, S. M., Frieling, J.,
660 Goldner, A., Hilgen, F. J., Kip, E. L., Peterse, F., Ploeg, R. van der, Röhl, U., Schouten, S., and
661 Sluijs, A.: Synchronous tropical and polar temperature evolution in the Eocene, *Nature*, 559,
662 382–386, <https://doi.org/10.1038/s41586-018-0272-2>, 2018.
- 663 Cramwinckel, M, et al. Burls, N.J., Fahad, A.A., Knapp, S., West, C.K., Reichgelt, T.,
664 Greenwood, D.R., Chan, W-L., Donnadieu, Y., Hutchinson, D., de Boer, A.M., Ladant, J-B.,
665 Morozova, P.A., Niezgodzki, I., Knorr, G., Steinig, S., Zhang, Z., Zhu, J., Feng, R., Lunt, D.J.,
666 Abe-Ouchi, A., and Inglis, G.N (2023) Paleobotanical-derived mean annual precipitation (MAT)
667 estimates for the early Eocene (56 to 48 million years ago) (Version 1) [Dataset] OSF.
668 <https://doi.org/10.17605/OSF.IO/M7B4K>
- 669
- 670 van Dijk, J., Fernandez, A., Bernasconi, S. M., Caves Rugenstein, J. K., Passey, S. R., and
671 White, T.: Spatial pattern of super-greenhouse warmth controlled by elevated specific humidity,
672 *Nat. Geosci.*, 13, 739–744, <https://doi.org/10.1038/s41561-020-00648-2>, 2020.
- 673 Eberle, J. J. and Greenwood, D. R.: Life at the top of the greenhouse Eocene world—A review of
674 the Eocene flora and vertebrate fauna from Canada's High Arctic, *Geol. Soc. Am. Bull.*, 124, 3–
675 23, <https://doi.org/10.1130/B30571.1>, 2012.
- 676 Eisawi, A. and Schrank, E.: Upper Cretaceous to Neogene palynology of the Melut Basin,
677 Southeast Sudan, *Palynology*, 32, 101–129, <https://doi.org/10.1080/01916122.2008.9989653>,
678 2008.

- 679 Evans, D., Sagoo, N., Renema, W., Cotton, L. J., Müller, W., Todd, J. A., Saraswati, P. K.,
680 Stassen, P., Ziegler, M., Pearson, P. N., Valdes, P. J., and Affek, H. P.: Eocene greenhouse
681 climate revealed by coupled clumped isotope-Mg/Ca thermometry, *Proc. Natl. Acad. Sci.*,
682 201714744, <https://doi.org/10.1073/pnas.1714744115>, 2018.
- 683 Eyring, V., Bony, S., Meehl, G. A., Senior, C. A., Stevens, B., Stouffer, R. J., and Taylor, K. E.:
684 Overview of the Coupled Model Intercomparison Project Phase 6 (CMIP6) experimental design
685 and organization, *Geosci. Model Dev.*, 9, 1937–1958, <https://doi.org/10.5194/gmd-9-1937-2016>,
686 2016.
- 687 Fauquette, S., Guiot, J., and Suc, J.-P.: A method for climatic reconstruction of the
688 Mediterranean Pliocene using pollen data, *Palaeogeogr. Palaeoclimatol. Palaeoecol.*, 144, 183–
689 201, [https://doi.org/10.1016/S0031-0182\(98\)00083-2](https://doi.org/10.1016/S0031-0182(98)00083-2), 1998.
- 690 Frederiksen, N. O.: Middle and late paleocene angiosperm pollen from Pakistan, *Palynology*, 18,
691 91–137, <https://doi.org/10.1080/01916122.1994.9989442>, 1994.
- 692 Garel, S., Schnyder, J., Jacob, J., Dupuis, C., Boussafir, M., Le Milbeau, C., Storme, J.-Y.,
693 Iakovleva, A. I., Yans, J., Baudin, F., Fléhoc, C., and Quesnel, F.: Paleohydrological and
694 paleoenvironmental changes recorded in terrestrial sediments of the Paleocene–Eocene
695 boundary (Normandy, France), *Palaeogeogr. Palaeoclimatol. Palaeoecol.*, 376, 184–199,
696 <https://doi.org/10.1016/j.palaeo.2013.02.035>, 2013.
- 697 Gaskell, D. E., Huber, M., O'Brien, C. L., Inglis, G. N., Acosta, R. P., Poulsen, C. J., and Hull, P.
698 M.: The latitudinal temperature gradient and its climate dependence as inferred from foraminiferal
699 $\delta^{18}\text{O}$ over the past 95 million years, *Proc. Natl. Acad. Sci.*, 119, e2111332119,
700 <https://doi.org/10.1073/pnas.2111332119>, 2022.
- 701 Givnish, T. J.: Leaf and Canopy Adaptations in Tropical Forests, in: *Physiological ecology of*
702 *plants of the wet tropics*, vol. 12, edited by: Medina, E., Mooney, H. A., and Vázquez-Yánes, C.,
703 Springer Netherlands, Dordrecht, 51–84, https://doi.org/10.1007/978-94-009-7299-5_6, 1984.

- 704 Graham, A., Cozadd, D., Areces-Mallea, A., and Frederiksen, N. O.: Studies in Neotropical
705 paleobotany. XIV. A palynoflora from the Middle Eocene Saramaguacán Formation of Cuba, *Am.*
706 *J. Bot.*, 87, 1526–1539, <https://doi.org/10.2307/2656879>, 2000.
- 707 Greenwood, D. R.: Fossil angiosperm leaves and climate: from Wolfe and Dilcher to Burnham
708 and Wilf, *Cour. Forschungsinstitut Senckenberg*, 258, 95–108, 2007.
- 709 Greenwood, D. R., Moss, P. T., Rowett, A. I., Vadala, A. J., and Keefe, R. L.: Plant communities
710 and climate change in southeastern Australia during the early Paleogene, in: Causes and
711 consequences of globally warm climates in the early Paleogene, edited by: Wing, S. L.,
712 Gingerich, P. D., Schmitz, B., and Thomas, E., Geological Society of America, 365–380, 2003.
- 713 Hailemichael, M., Aronson, J. L., Savin, S., Tevesz, M. J. S., and Carter, J. G.: $\delta^{18}\text{O}$ in mollusk
714 shells from Pliocene Lake Hadar and modern Ethiopian lakes: implications for history of the
715 Ethiopian monsoon, *Palaeogeogr. Palaeoclimatol. Palaeoecol.*, 186, 81–99,
716 [https://doi.org/10.1016/S0031-0182\(02\)00445-5](https://doi.org/10.1016/S0031-0182(02)00445-5), 2002.
- 717 Handley, L., O'Halloran, A., Pearson, P. N., Hawkins, E., Nicholas, C. J., Schouten, S., McMillan,
718 I. K., and Pancost, R. D.: Changes in the hydrological cycle in tropical East Africa during the
719 Paleocene–Eocene Thermal Maximum, *Palaeogeogr. Palaeoclimatol. Palaeoecol.*, 329–330, 10–
720 21, <https://doi.org/10.1016/j.palaeo.2012.02.002>, 2012.
- 721 Harper, D. T., Zeebe, R., Hönisch, B., Schrader, C. D., Lourens, L. J., and Zachos, J. C.:
722 Subtropical sea-surface warming and increased salinity during Eocene Thermal Maximum 2,
723 *Geology*, 46, 187–190, <https://doi.org/10.1130/G39658.1>, 2017.
- 724 Held, I. M. and Soden, B. J.: Robust Responses of the Hydrological Cycle to Global Warming, *J.*
725 *Clim.*, 19, 5686–5699, <https://doi.org/10.1175/JCLI3990.1>, 2006.
- 726 Herman, A. B., Spicer, R. A., Aleksandrova, G. N., Yang, J., Kodrul, T. M., Maslova, N. P.,
727 Spicer, T. E. V., Chen, G., and Jin, J.-H.: Eocene–early Oligocene climate and vegetation

- 728 change in southern China: Evidence from the Maoming Basin, *Palaeogeogr. Palaeoclimatol.*
729 *Palaeoecol.*, 479, 126–137, <https://doi.org/10.1016/j.palaeo.2017.04.023>, 2017.
- 730 Herold, N., Buzan, J., Seton, M., Goldner, A., Green, J. A. M., Müller, R. D., Markwick, P., and
731 Huber, M.: A suite of early Eocene (~ 55 Ma) climate model boundary conditions, *Geosci Model*
732 *Dev.*, 7, 2077–2090, <https://doi.org/10.5194/gmd-7-2077-2014>, 2014.
- 733 Hijmans, R. J., Phillips, S., Leathwick, J., and Elith, J.: *dismo: Species Distribution Modeling*,
734 2020.
- 735 Hoegh-Guldberg, O., Jacob, D., Taylor, M., Bindi, M., Brown, S., Camilloni, I., Diedhiou, A.,
736 Djalante, R., Ebi, K. L., Engelbrecht, F., Guiot, J., Hijioka, Y., Mehrotra, S., Payne, A.,
737 Seneviratne, S. I., Thomas, A., Warren, R., and Zhou, G.: Impacts of 1.5°C Global Warming on
738 Natural and Human Systems, in: *Global Warming of 1.5°C. An IPCC Special Report on the*
739 *impacts of global warming of 1.5°C above pre-industrial levels and related global greenhouse*
740 *gas emission pathways, in the context of strengthening the global response to the threat of*
741 *climate change, sustainable development, and efforts to eradicate poverty*, edited by: Masson-
742 Delmotte, V., Zhai, P., Pörtner, H.-O., Roberts, D., Skea, J., Shukla, P. R., Pirani, A., Moufouma-
743 Okia, W., Péan, C., Pidcock, R., Connors, S., Matthews, J. B. R., Chen, Y., Zhou, X., Gomis, M.
744 I., Lonnoy, E., Maycock, T., Tignor, M., and Waterfield, T., In press, 2018.
- 745 Hollis, C.J., Dunkley Jones, T., Anagnostou, E., Bijl, P.K., Cramwinckel, M.J., Cui, Y., Dickens,
746 G.R., Edgar, K.M., Eley, Y., Evans, D., Foster, G.L., Frieling, J., Inglis, G.N., Kennedy, E.M.,
747 Kozdon, R., Lauretano, V., Lear, C.H., Littler, K., Lourens, L., Meckler, A.N., Naafs, B.D.A.,
748 Pälke, H., Pancost, R.D., Pearson, P.N., Röhl, U., Royer, D.L., Salzmann, U., Schubert, B.A.,
749 Seebeck, H., Sluijs, A., Speijer, R.P., Stassen, P., Tierney, J., Tripathi, A., Wade, B., Westerhold,
750 T., Witkowski, C., Zachos, J.C., Zhang, Y.G., Huber, M. and Lunt, D.J. (2019b) The DeepMIP
751 contribution to PMIP4: methodologies for selection, compilation and analysis of latest Paleocene
752 and early Eocene climate proxy data, incorporating version 0.1 of the DeepMIP database.
753 *Geosci. Model Dev.* 12, 3149-3206

- 754 Inglis, G. N., Bragg, F., Burls, N. J., Cramwinckel, M. J., Evans, D., Foster, G. L., Huber, M.,
755 Lunt, D. J., Siler, N., Steinig, S., Tierney, J. E., Wilkinson, R., Anagnostou, E., de Boer, A. M.,
756 Dunkley Jones, T., Edgar, K. M., Hollis, C. J., Hutchinson, D. K., and Pancost, R. D.: Global
757 mean surface temperature and climate sensitivity of the early Eocene Climatic Optimum (EECO),
758 Paleocene–Eocene Thermal Maximum (PETM), and latest Paleocene, *Clim. Past*, 16, 1953–
759 1968, <https://doi.org/10.5194/cp-16-1953-2020>, 2020.
- 760 Jaramillo, C. A., Bayona, G., Pardo-Trujillo, A., Rueda, M., Torres, V., Harrington, G. J., and
761 Mora, G.: THE PALYNOLOGY OF THE CERREJÓN FORMATION (UPPER PALEOCENE) OF
762 NORTHERN COLOMBIA, *Palynology*, 31, 153–189, <https://doi.org/10.2113/gspalynol.31.1.153>,
763 2007.
- 764 Jarzen, D. M. and Klug, C.: A preliminary investigation of a lower to middle Eocene palynoflora
765 from Pine Island, Florida, USA, *Palynology*, 34, 164–179,
766 <https://doi.org/10.1080/01916121003737421>, 2010.
- 767 Kender, S., Stephenson, M. H., Riding, J. B., Leng, M. J., Knox, R. W. O., Peck, V. L., Kendrick,
768 C. P., Ellis, M. A., Vane, C. H., and Jamieson, R.: Marine and terrestrial environmental changes
769 in NW Europe preceding carbon release at the Paleocene–Eocene transition, *Earth Planet. Sci.*
770 *Lett.*, 353–354, 108–120, <https://doi.org/10.1016/j.epsl.2012.08.011>, 2012.
- 771 Kennedy, E. M., Arens, N. C., Reichgelt, T., Spicer, R. A., Spicer, T. E. V., Stranks, L., and Yang,
772 J.: Deriving temperature estimates from Southern Hemisphere leaves, *Palaeogeogr.*
773 *Palaeoclimatol. Palaeoecol.*, 412, 80–90, <https://doi.org/10.1016/j.palaeo.2014.07.015>, 2014.
- 774 Kraus, M. J. and Riggins, S.: Transient drying during the Paleocene–Eocene Thermal Maximum
775 (PETM): Analysis of paleosols in the bighorn basin, Wyoming, *Palaeogeogr. Palaeoclimatol.*
776 *Palaeoecol.*, 245, 444–461, <https://doi.org/10.1016/j.palaeo.2006.09.011>, 2007.
- 777 Kraus, M. J., McInerney, F. A., Wing, S. L., Secord, R., Baczynski, A. A., and Bloch, J. I.:
778 Paleohydrologic response to continental warming during the Paleocene–Eocene Thermal

- 779 Maximum, Bighorn Basin, Wyoming, *Palaeogeogr. Palaeoclimatol. Palaeoecol.*, 370, 196–208,
780 <https://doi.org/10.1016/j.palaeo.2012.12.008>, 2013.
- 781 Lunt, D. J., Bragg, F., Chan, W.-L., Hutchinson, D. K., Ladant, J.-B., Morozova, P., Niezgodzki, I.,
782 Steinig, S., Zhang, Z., Zhu, J., Abe-Ouchi, A., Anagnostou, E., de Boer, A. M., Coxall, H. K.,
783 Donnadieu, Y., Foster, G., Inglis, G. N., Knorr, G., Langebroek, P. M., Lear, C. H., Lohmann, G.,
784 Poulsen, C. J., Sepulchre, P., Tierney, J. E., Valdes, P. J., Volodin, E. M., Dunkley Jones, T.,
785 Hollis, C. J., Huber, M., and Otto-Bliesner, B. L.: DeepMIP: model intercomparison of early
786 Eocene climatic optimum (EECO) large-scale climate features and comparison with proxy data,
787 *Clim. Past*, 17, 203–227, <https://doi.org/10.5194/cp-17-203-2021>, 2021.
- 788 Lunt, D. J (2023, March 11th) The DeepMIP model database (version 1.0) [Dataset] University of
789 Bristol Research Data Storage Facility (RDSF). <https://www.deepmip.org/data-eocene/>.
- 790 Masson-Delmotte, V., Zhai, P., Pirani, A., Connors, S. L., Péan, C., Chen, Y., Goldfarb, L.,
791 Gomis, M. I., Matthews, J. B. R., Berger, S., Huang, M., Yelekçi, O., Yu, R., Zhou, B., Lonnoy, E.,
792 Maycock, T. K., Waterfield, T., and Leitzell, K.: IPCC, 2021: Climate Change 2021: The Physical
793 Science Basis. Contribution of Working Group I to the Sixth Assessment Report of the
794 Intergovernmental Panel on Climate Change, Cambridge University Press, Cambridge, United
795 Kingdom and New York, NY, USA, 2022.
- 796 Mosbrugger, V. and Utescher, T.: The coexistence approach — a method for quantitative
797 reconstructions of Tertiary terrestrial palaeoclimate data using plant fossils, *Palaeogeogr.*
798 *Palaeoclimatol. Palaeoecol.*, 134, 61–86, [https://doi.org/10.1016/S0031-0182\(96\)00154-X](https://doi.org/10.1016/S0031-0182(96)00154-X), 1997.
- 799 Pagani, M., Pedentchouk, N., Huber, M., Sluijs, A., Schouten, S., Brinkhuis, H., Sinninghe
800 Damsté, J. S., Dickens, G. R., Expedition 302 Scientists, Backman, J., Clemens, S., Cronin, T.,
801 Eynaud, F., Gattacceca, J., Jakobsson, M., Jordan, R., Kaminski, M., King, J., Koc, N., Martinez,
802 N. C., McInroy, D., Jr, T. C. M., O'Regan, M., Onodera, J., Pälike, H., Rea, B., Rio, D.,
803 Sakamoto, T., Smith, D. C., John, K. E. K. S., Suto, I., Suzuki, N., Takahashi, K., Watanabe, M.,

804 and Yamamoto, M.: Arctic hydrology during global warming at the Palaeocene/Eocene thermal
805 maximum, *Nature*, 442, 671–675, <https://doi.org/10.1038/nature05043>, 2006.

806 Pancost, R. D., Taylor, K. W. R., Inglis, G. N., Kennedy, E. M., Handley, L., Hollis, C. J., Crouch,
807 E. M., Pross, J., Huber, M., Schouten, S., Pearson, P. N., Morgans, H. E. G., and Raine, J. I.:
808 Early Paleogene evolution of terrestrial climate in the SW Pacific, Southern New Zealand,
809 *Geochem. Geophys. Geosystems*, 14, 5413–5429, <https://doi.org/10.1002/2013GC004935>,
810 2013.

811 Pardo-Trujillo, A., Jaramillo, C. A., and Oboh-Ikuenobe, F. E.: Paleogene palynostratigraphy of
812 the eastern middle Magdalena Valley, Colombia, *Palynology*, 27, 155–178,
813 <https://doi.org/10.1080/01916122.2003.9989585>, 2003.

814 Pendergrass, A. G.: The Global-Mean Precipitation Response to CO₂-Induced Warming in
815 CMIP6 Models, *Geophys. Res. Lett.*, 47, e2020GL089964,
816 <https://doi.org/10.1029/2020GL089964>, 2020.

817 Peppe, D. J., Royer, D. L., Cariglino, B., Oliver, S. Y., Newman, S., Leight, E., Enikolopov, G.,
818 Fernandez-Burgos, M., Herrera, F., Adams, J. M., Correa, E., Currano, E. D., Erickson, J. M.,
819 Hinojosa, L. F., Hoganson, J. W., Iglesias, A., Jaramillo, C. A., Johnson, K. R., Jordan, G. J.,
820 Kraft, N. J. B., Lovelock, E. C., Lusk, C. H., Niinemets, Ü., Peñuelas, J., Rapson, G., Wing, S. L.,
821 and Wright, I. J.: Sensitivity of leaf size and shape to climate: global patterns and paleoclimatic
822 applications, *New Phytol.*, 190, 724–739, <https://doi.org/10.1111/j.1469-8137.2010.03615.x>,
823 2011.

824 Poole, I. and van Bergen, P. F.: Physiognomic and chemical characters in wood as
825 palaeoclimate proxies, in: *Plants and Climate Change*, edited by: Rozema, J., Aerts, R., and
826 Cornelissen, H., Springer Netherlands, Dordrecht, 175–196, [https://doi.org/10.1007/978-1-4020-](https://doi.org/10.1007/978-1-4020-4443-4_12)
827 [4443-4_12](https://doi.org/10.1007/978-1-4020-4443-4_12), 2006.

- 828 Poole, I., Cantrill, D., and Utescher, T.: A multi-proxy approach to determine Antarctic terrestrial
829 palaeoclimate during the Late Cretaceous and Early Tertiary, *Palaeogeogr. Palaeoclimatol.*
830 *Palaeoecol.*, 222, 95–121, <https://doi.org/10.1016/j.palaeo.2005.03.011>, 2005.
- 831 Pross, J., Klotz, S., and Mosbrugger, V.: Reconstructing palaeotemperatures for the Early and
832 Middle Pleistocene using the mutual climatic range method based on plant fossils, *Quat. Sci.*
833 *Rev.*, 19, 1785–1799, [https://doi.org/10.1016/S0277-3791\(00\)00089-5](https://doi.org/10.1016/S0277-3791(00)00089-5), 2000.
- 834 Pross, J., Contreras, L., Bijl, P. K., Greenwood, D. R., Bohaty, S. M., Schouten, S., Bendle, J. A.,
835 Röhl, U., Tauxe, L., Raine, J. I., Huck, C. E., van de Flierdt, T., Jamieson, S. S. R., Stickley, C.
836 E., van de Schootbrugge, B., Escutia, C., Brinkhuis, H., and Scientists, I. O. D. P. E. 318:
837 Persistent near-tropical warmth on the Antarctic continent during the early Eocene epoch,
838 *Nature*, 488, 73–77, <https://doi.org/10.1038/nature11300>, 2012.
- 839 Quattrocchio, M. E. and Volkheimer, W.: Paleoclimatic Changes during the Paleocene-Lower
840 Eocene in the Salta Group Basin, NW Argentina, in: *Southern Hemisphere Paleo- and*
841 *Neoclimates: Key Sites, Methods, Data and Models*, edited by: Smolka, P. and Volkheimer, W.,
842 Springer, Berlin, Heidelberg, 353–367, https://doi.org/10.1007/978-3-642-59694-0_22, 2000.
- 843 Reichgelt, T., Kennedy, E. M., Conran, J. G., Lee, W. G., and Lee, D. E.: The presence of
844 moisture deficits in Miocene New Zealand, *Glob. Planet. Change*, 172, 268–277,
845 <https://doi.org/10.1016/j.gloplacha.2018.10.013>, 2019.
- 846 Reichgelt, T., Greenwood, D. R., Steinig, S., Conran, J. G., Hutchinson, D. K., Lunt, D. J.,
847 Scriven, L. J., and Zhu, J.: Plant Proxy Evidence for High Rainfall and Productivity in the Eocene
848 of Australia, *Paleoceanogr. Paleoclimatology*, 37, e2022PA004418,
849 <https://doi.org/10.1029/2022PA004418>, 2022.
- 850 Salpin, M., Schnyder, J., Baudin, F., Suan, G., Suc, J.-P., Popescu, S.-M., Fauquette, S.,
851 Reinhardt, L., Schmitz, M. D., and Labrousse, L.: Evidence for subtropical warmth in the
852 Canadian Arctic (Beaufort-Mackenzie, Northwest Territories, Canada) during the early Eocene,
853 [https://doi.org/10.1130/2018.2541\(27\)](https://doi.org/10.1130/2018.2541(27)), 2019.

- 854 Schuster, M., Düringer, P., Ghienne, J.-F., Roquin, C., Sepulchre, P., Moussa, A., Lebatard, A.-
855 E., Mackaye, H. T., Likius, A., Vignaud, P., and Brunet, M.: Chad Basin: Paleoenvironments of
856 the Sahara since the Late Miocene, *Comptes Rendus Geosci.*, 341, 603–611,
857 <https://doi.org/10.1016/j.crte.2009.04.001>, 2009.
- 858 Seager, R. and Henderson, N.: Diagnostic Computation of Moisture Budgets in the ERA-Interim
859 Reanalysis with Reference to Analysis of CMIP-Archived Atmospheric Model Data, *J. Clim.*, 26,
860 7876–7901, <https://doi.org/10.1175/JCLI-D-13-00018.1>, 2013.
- 861 Seager, R., Naik, N., and Vecchi, G. A.: Thermodynamic and Dynamic Mechanisms for Large-
862 Scale Changes in the Hydrological Cycle in Response to Global Warming, *J. Clim.*, 23, 4651–
863 4668, <https://doi.org/10.1175/2010JCLI3655.1>, 2010.
- 864 Shukla, A., Mehrotra, R. C., Spicer, R. A., Spicer, T. E. V., and Kumar, M.: Cool equatorial
865 terrestrial temperatures and the South Asian monsoon in the Early Eocene: Evidence from the
866 Gurha Mine, Rajasthan, India, *Palaeogeogr. Palaeoclimatol. Palaeoecol.*, 412, 187–198,
867 <https://doi.org/10.1016/j.palaeo.2014.08.004>, 2014.
- 868 Siler, N., Roe, G. H., Armour, K. C., and Feldl, N.: Revisiting the surface-energy-flux perspective
869 on the sensitivity of global precipitation to climate change, *Clim. Dyn.*, 52, 3983–3995,
870 <https://doi.org/10.1007/s00382-018-4359-0>, 2019.
- 871 Slingo, J., Bates, P., Bauer, P., Belcher, S., Palmer, T., Stephens, G., Stevens, B., Stocker, T.,
872 and Teutsch, G.: Ambitious partnership needed for reliable climate prediction, *Nat. Clim. Change*,
873 12, 499–503, <https://doi.org/10.1038/s41558-022-01384-8>, 2022.
- 874 Sluijs, A., Bijl, P. K., Schouten, S., Röhl, U., Reichert, G.-J., and Brinkhuis, H.: Southern ocean
875 warming, sea level and hydrological change during the Paleocene-Eocene thermal maximum,
876 *Clim Past*, 7, 47–61, <https://doi.org/10.5194/cp-7-47-2011>, 2011.

- 877 Smith, F. A., Wing, S. L., and Freeman, K. H.: Magnitude of the carbon isotope excursion at the
878 Paleocene–Eocene thermal maximum: The role of plant community change, *Earth Planet. Sci.*
879 *Lett.*, 262, 50–65, <https://doi.org/10.1016/j.epsl.2007.07.021>, 2007.
- 880 Smith, V., Warny, S., Jarzen, D. M., Demchuk, T., Vajda, V., and Gulick, S. P. S.: Paleocene–
881 Eocene palynomorphs from the Chicxulub impact crater, Mexico. Part 2: angiosperm pollen,
882 *Palynology*, 44, 489–519, <https://doi.org/10.1080/01916122.2019.1705417>, 2020.
- 883 Sniderman, J. M. K., Woodhead, J. D., Hellstrom, J., Jordan, G. J., Drysdale, R. N., Tyler, J. J.,
884 and Porch, N.: Pliocene reversal of late Neogene aridification, *Proc. Natl. Acad. Sci.*, 113, 1999–
885 2004, <https://doi.org/10.1073/pnas.1520188113>, 2016.
- 886 Spicer, R. A., Yang, J., Spicer, T. E. V., and Farnsworth, A.: Woody dicot leaf traits as a
887 palaeoclimate proxy: 100 years of development and application, *Palaeogeogr. Palaeoclimatol.*
888 *Palaeoecol.*, 562, 110138, <https://doi.org/10.1016/j.palaeo.2020.110138>, 2021.
- 889 Su, T., Spicer, R. A., Wu, F.-X., Farnsworth, A., Huang, J., Rio, C. D., Deng, T., Ding, L., Deng,
890 W.-Y.-D., Huang, Y.-J., Hughes, A., Jia, L.-B., Jin, J.-H., Li, S.-F., Liang, S.-Q., Liu, J., Liu, X.-Y.,
891 Sherlock, S., Spicer, T., Srivastava, G., Tang, H., Valdes, P., Wang, T.-X., Widdowson, M., Wu,
892 M.-X., Xing, Y.-W., Xu, C.-L., Yang, J., Zhang, C., Zhang, S.-T., Zhang, X.-W., Zhao, F., and
893 Zhou, Z.-K.: A Middle Eocene lowland humid subtropical “Shangri-La” ecosystem in central Tibet,
894 *Proc. Natl. Acad. Sci.*, 117, 32989–32995, <https://doi.org/10.1073/pnas.2012647117>, 2020.
- 895 Suan, G., Popescu, S.-M., Suc, J.-P., Schnyder, J., Fauquette, S., Baudin, F., Yoon, D.,
896 Piepjohn, K., Sobolev, N. N., and Labrousse, L.: Subtropical climate conditions and mangrove
897 growth in Arctic Siberia during the early Eocene, *Geology*, 45, 539–542,
898 <https://doi.org/10.1130/G38547.1>, 2017.
- 899 Teodoridis, V., Mazouch, P., Spicer, R. A., and Uhl, D.: Refining CLAMP — Investigations
900 towards improving the Climate Leaf Analysis Multivariate Program, *Palaeogeogr. Palaeoclimatol.*
901 *Palaeoecol.*, 299, 39–48, <https://doi.org/10.1016/j.palaeo.2010.10.031>, 2011.

- 902 Tian, B. and Dong, X.: The Double-ITCZ Bias in CMIP3, CMIP5, and CMIP6 Models Based on
903 Annual Mean Precipitation, *Geophys. Res. Lett.*, 47, e2020GL087232,
904 <https://doi.org/10.1029/2020GL087232>, 2020.
- 905 Tierney, J. E., Zhu, J., Li, M., Ridgwell, A., Hakim, G. J., Poulsen, C. J., Whiteford, R. D. M., Rae,
906 J. W. B., and Kump, L. R.: Spatial patterns of climate change across the Paleocene–Eocene
907 Thermal Maximum, *Proc. Natl. Acad. Sci.*, 119, e2205326119,
908 <https://doi.org/10.1073/pnas.2205326119>, 2022.
- 909 Trenberth, K. E. and Guillemot, C. J.: Evaluation of the Global Atmospheric Moisture Budget as
910 Seen from Analyses, *J. Clim.*, 8, 2255–2272, [https://doi.org/10.1175/1520-0442\(1995\)008<2255:EOTGAM>2.0.CO;2](https://doi.org/10.1175/1520-0442(1995)008<2255:EOTGAM>2.0.CO;2), 1995.
- 912 Tripathi, S. K. M., Saxena, R. K., and Prasad, V.: Palynological investigation of the tura formation
913 (early eocene) exposed along the tura-dalu road, west Garo Hills, Meghalaya, India, 2000.
- 914 Verma, P., Garg, R., Rao, M. R., and Bajpai, S.: Palynofloral diversity and palaeoenvironments of
915 early Eocene Akri lignite succession, Kutch Basin, western India, *Palaeobiodiversity*
916 *Palaeoenvironments*, <https://doi.org/10.1007/s12549-019-00388-1>, 2019.
- 917 Wang, H., Lu, H., Zhao, L., Zhang, H., Lei, F., and Wang, Y.: Asian monsoon rainfall variation
918 during the Pliocene forced by global temperature change, *Nat. Commun.*, 10, 5272,
919 <https://doi.org/10.1038/s41467-019-13338-4>, 2019.
- 920 West, C. K., Greenwood, D. R., and Basinger, J. F.: Was the Arctic Eocene ‘rainforest’
921 monsoonal? Estimates of seasonal precipitation from early Eocene megafloras from Ellesmere
922 Island, Nunavut, *Earth Planet. Sci. Lett.*, 427, 18–30, <https://doi.org/10.1016/j.epsl.2015.06.036>,
923 2015.
- 924 West, C. K., Greenwood, D. R., Reichgelt, T., Lowe, A. J., Vachon, J. M., and Basinger, J. F.:
925 Paleobotanical proxies for early Eocene climates and ecosystems in northern North America

- 926 from middle to high latitudes, *Clim. Past*, 16, 1387–1410, [https://doi.org/10.5194/cp-16-1387-](https://doi.org/10.5194/cp-16-1387-2020)
927 2020, 2020.
- 928 Wiemann, M. C., Wheeler, E. A., Manchester, S. R., and Portier, K. M.: Dicotyledonous wood
929 anatomical characters as predictors of climate, *Palaeogeogr. Palaeoclimatol. Palaeoecol.*, 139,
930 83–100, [https://doi.org/10.1016/S0031-0182\(97\)00100-4](https://doi.org/10.1016/S0031-0182(97)00100-4), 1998.
- 931 Wilf, P., Wing, S. L., Greenwood, D. R., and Greenwood, C. L.: Using fossil leaves as
932 paleoprecipitation indicators: An Eocene example, *Geology*, 26, 203–206,
933 [https://doi.org/10.1130/0091-7613\(1998\)026<0203:UFLAPI>2.3.CO;2](https://doi.org/10.1130/0091-7613(1998)026<0203:UFLAPI>2.3.CO;2), 1998.
- 934 Willard, D. A., Donders, T. H., Reichgelt, T., Greenwood, D. R., Sangiorgi, F., Peterse, F.,
935 Nierop, K. G. J., Frieling, J., Schouten, S., and Sluijs, A.: Arctic vegetation, temperature, and
936 hydrology during Early Eocene transient global warming events, *Glob. Planet. Change*, 178,
937 139–152, <https://doi.org/10.1016/j.gloplacha.2019.04.012>, 2019.
- 938 Williams, C. J. R., Lunt, D. J., Salzmann, U., Reichgelt, T., Inglis, G. N., Greenwood, D. R.,
939 Chan, W.-L., Abe-Ouchi, A., Donnadieu, Y., Hutchinson, D. K., de Boer, A. M., Ladant, J.-B.,
940 Morozova, P. A., Niezgodzki, I., Knorr, G., Steinig, S., Zhang, Z., Zhu, J., Huber, M., and Otto-
941 Bliesner, B. L.: African Hydroclimate During the Early Eocene From the DeepMIP Simulations,
942 *Paleoceanogr. Paleoclimatology*, 37, e2022PA004419, <https://doi.org/10.1029/2022PA004419>,
943 2022.
- 944 Wing, S. L. and Greenwood, D. R.: Fossils and fossil climate: the case for equable continental
945 interiors in the Eocene, *Philos. Trans. R. Soc. Lond. B. Biol. Sci.*, 341, 243–252,
946 <https://doi.org/10.1098/rstb.1993.0109>, 1993.
- 947 Wing, S. L., Herrera, F., Jaramillo, C. A., Gómez-Navarro, C., Wilf, P., and Labandeira, C. C.:
948 Late Paleocene fossils from the Cerrejón Formation, Colombia, are the earliest record of
949 Neotropical rainforest, *Proc. Natl. Acad. Sci.*, 106, 18627–18632,
950 <https://doi.org/10.1073/pnas.0905130106>, 2009.

- 951 Wolfe, J. A.: A Method of Obtaining Climatic Parameters from Leaf Assemblages, U.S.
952 Government Printing Office, 360 pp., 1993.
- 953 Wolfe, J. A.: Paleoclimatic Estimates from Tertiary Leaf Assemblages, *Annu. Rev. Earth Planet.*
954 *Sci.*, 23, 119–142, <https://doi.org/10.1146/annurev.ea.23.050195.001003>, 1995.
- 955 Xie, Y., Wu, F., Fang, X., Zhang, D., and Zhang, W.: Early Eocene southern China dominated by
956 desert: Evidence from a palynological record of the Hengyang Basin, Hunan Province, *Glob.*
957 *Planet. Change*, 195, 103320, <https://doi.org/10.1016/j.gloplacha.2020.103320>, 2020.
- 958 Yang, J., Spicer, R. A., Spicer, T. E. V., Arens, N. C., Jacques, F. M. B., Su, T., Kennedy, E. M.,
959 Herman, A. B., Steart, D. C., Srivastava, G., Mehrotra, R. C., Valdes, P. J., Mehrotra, N. C.,
960 Zhou, Z.-K., and Lai, J.-S.: Leaf form–climate relationships on the global stage: an ensemble of
961 characters, *Glob. Ecol. Biogeogr.*, 24, 1113–1125, <https://doi.org/10.1111/geb.12334>, 2015.
- 962 Zhang, R., Yan, Q., Zhang, Z. S., Jiang, D., Otto-Bliesner, B. L., Haywood, A. M., Hill, D. J.,
963 Dolan, A. M., Stepanek, C., Lohmann, G., Contoux, C., Bragg, F., Chan, W.-L., Chandler, M. A.,
964 Jost, A., Kamae, Y., Abe-Ouchi, A., Ramstein, G., Rosenbloom, N. A., Sohl, L., and Ueda, H.:
965 Mid-Pliocene East Asian monsoon climate simulated in the PlioMIP, *Clim. Past*, 9, 2085–2099,
966 <https://doi.org/10.5194/cp-9-2085-2013>, 2013.
- 967
- 968

969 **Figure Captions**

970

971 **Figure 1. Overview of early Eocene precipitation proxy compilation.** Previously
972 published estimates compiled by the Carmichael et al., (2016) shown as purple squares;
973 additional published estimates plotted as dark green circles; new estimates (*this study*)
974 plotted as light green circles. Sample locations plotted with their modern positions on a
975 present-day world map.

976

977 **Figure 2. Rainfall patterns in DeepMIP pre-industrial simulations.** **a)** Climate Prediction
978 Center (CPC) Merged Analysis of Precipitation (CMAP) Observations (Xie & Arkin 1997), **b)**
979 multi-model mean (MMM) of precipitation estimates (mm/day) for the pre-industrial control
980 runs for the 9 models in the DeepMIP ensemble (middle), **c)** MMM anomalies in precipitation
981 (mm/day) for DeepMIP pre-industrial control runs minus modern observations. **d)** Zonal-
982 mean precipitation of DeepMIP model control runs and modern observations. Note that the
983 MMM contains a different model ensemble for different CO₂ concentrations (see Table S1,
984 Figure 4).

985

986 **Figure 3. Global hydrological response to warming in the DeepMIP experiments.**
987 Global mean change in precipitation relative to pre-industrial (in % change) on the vertical
988 axis plotted against global mean surface air temperature (GMST) relative to pre-industrial (in
989 °C) on the horizontal axis. Simulations with the same model at three or more different CO₂
990 levels have been connected by coloured lines. Correlation coefficient of a linear fit through
991 the combined values (black line) is 0.96, slope is 2.4% increase in precipitation per °C of
992 warming.

993

994 **Figure 4. Multi-model mean temperature and precipitation anomalies relative to the**
995 **pre-industrial control in the DeepMIP simulations.** a) surface air temperature, b)
996 precipitation and c) precipitation – evaporation (P-E). "n" values above each plot represent

997 the number of models available for calculating the MMM. See Figure S7 for the standard
998 deviation in each variable across the ensemble members contributing to the ensemble mean
999

1000 **Figure 5. Mean annual precipitation (MAP) values in the DeepMIP Eocene simulations**
1001 **for the a) tropics (15°–15° N/S), b) subtropics (15°–30° N/S), c) mid latitudes (30°–60°**
1002 **N/S), and d) high latitudes (60°–90° N/S).** Panels (a-d) show the % change in MAP relative
1003 to pre-industrial vs the change in global mean surface air temperature change (GMST; °C)
1004 relative to pre-industrial. Simulations with the same model at 3 or more different CO₂ levels
1005 have been connected by colored lines. Dashed black line represents a linear fit through the
1006 combined values and the slope and correlation coefficient are shown in bottom right hand
1007 corner. Note that y-axis scaling differs between plots.

1008

1009 **Figure 6. Precipitation-evaporation ($P-E$) values in the DeepMIP model simulations**
1010 **for the a) tropics (15°–15° N/S), b) subtropics (15°–30° N/S), c) mid latitudes (30°–60°**
1011 **N/S), and d) high latitudes (60°–90° N/S).** Panels (a-d) show the change in $P-E$ relative to
1012 pre-industrial (mm/day) vs the change in global mean surface air temperature change
1013 (GMST; °C) relative to pre-industrial. Simulations with the same model at 3 or more different
1014 CO₂ levels have been connected by colored lines. Dashed black line represents a linear fit
1015 through the combined values and the slope and correlation coefficient are shown in bottom
1016 right hand corner Note that y-axis scaling differs between plots.

1017

1018 **Figure 7. Zonal-mean MAP and ITCZ characteristics in the DeepMIP-Eocene**
1019 **simulations.** a) The width of the ITCZ (defined as in Byrne and Schneider, 2016), b) the
1020 ITCZ latitude of maximum precipitation and c) the zonal-mean MAP profiles for each model.

1021

1022 **Figure 8. Zonal-mean components of the hydrological cycle as functions of latitude in**
1023 **the DeepMIP simulations.** a) surface precipitation minus evaporation ($P-E$), b) implied
1024 moisture transport (\overline{vq} implied in g/kg m/s), c) moisture transport by time-mean flow (\overline{vq} in

1025 g/kg m/s), d) moisture transport by eddy transport ($\overline{v'q'}$ in g/kg m/s), e) the contribution of
1026 changes in the time-mean humidity to changes in the moisture transport (i.e.,
1027 thermodynamic effects) ($\overline{v_{cnt}\delta q}$ in g/kg m/s), f) the contribution of changes in the circulation to
1028 changes in moisture transport (i.e., dynamic effects) ($\delta\overline{vq}_{cnt}$ in g/kg m/s). Full set of
1029 simulations is plotted as thin transparent colored lines, and the multi model mean as thick
1030 colored lines. Note that the MMM contains a different model ensemble for different CO₂
1031 concentrations (see Table S1, Figure 4). Note also that IPSL, INMCM, and NorESM are
1032 missing from the moisture budget analysis in this and subsequent plots because the
1033 atmospheric variables required were missing from the DeepMIP database.

1034

1035 **Figure 9. Subtropical moisture budget diagnostics show competing influence of**
1036 **atmospheric humidity and circulation in the subtropics (15-30°N/S).** a) the
1037 relationship between changes in subtropical $P-E$ and GMST, b) the relationship between
1038 changes in subtropical $P-E$ and the latitudinal temperature gradient (LTG) between
1039 15°S–15°N and 30–60°N/S, c) changes in subtropical $P-E$ due to humidity-induced
1040 changes in the time-mean moisture transport divergence (i.e., \overline{vq} implied in g/kg m/s), c)
1041 moisture transport by time-mean flow (\overline{vq} in g/kg m/s), d) changes in subtropical $P-E$ due
1042 to circulation-induced changes in the time-mean humidity to changes in the moisture
1043 transport (i.e., thermodynamic effects) ($\overline{v_{cnt}\delta q}$ in g/kg m/s), f) the contribution of changes in
1044 the circulation to changes in moisture transport (i.e., dynamic effects).

1045

1046 **Figure 10. Proxy-based mean annual precipitation (MAP; mm/day) values overlaid**
1047 **on simulated MAP fields from the DeepMIP ensemble.** (a) Zonal-mean MAP from all the
1048 DeepMIP-Eocene experiments (light coloured lines) with the multi-model-mean as a bold line
1049 and the proxy estimate overlaid as symbols (NLR-based approaches in black; LAA in dark
1050 grey; CLAMP in light grey). See Figure S10 for individual model plots with simulated MAP
1051 values at the proxy locations rather than zonal-mean values. (b) MMM MAP for each
1052 DeepMIP-Eocene CO₂ experiment with the reconstructed MAP estimates overlaid.

1053

1054 **Figure 11. Data-model comparison for the early Eocene.** In each panel, the early Eocene
1055 multi-model-mean (MMM) mean annual precipitation (MAP) bias is shown for a given CO₂
1056 concentration. The root-mean-square error of the bias across all the sites is shown in black
1057 on the left. Lower values indicate a closer data-model agreement.

1058

1059 **Figure 12. Zonally-averaged model-data mean annual precipitation (MAP) bias for the**
1060 **a) tropics (15°–15° N/S), b) subtropics (15°–30° N/S), c) mid latitudes (30°–60° N/S), and**
1061 **d) high latitudes (60°–90° N/S).** Panels (a-d) show the model-data bias in mm/day for the
1062 different model simulations, sorted by CO₂ forcing

1063

Figure 1.

Key: ■ Carmichael et al., 2016 ● Existing data ● New data

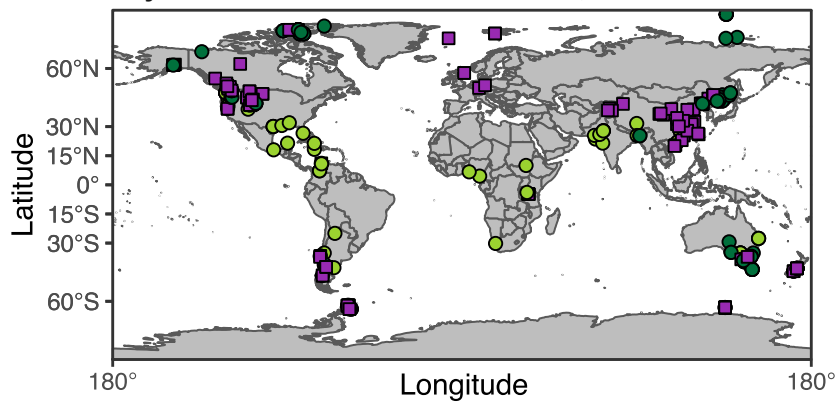


Figure 2.

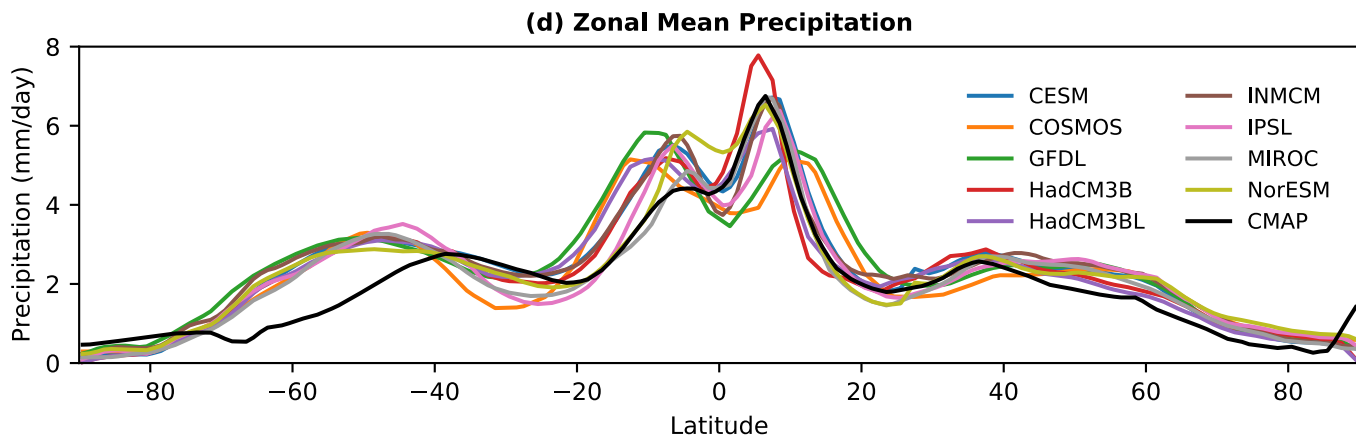
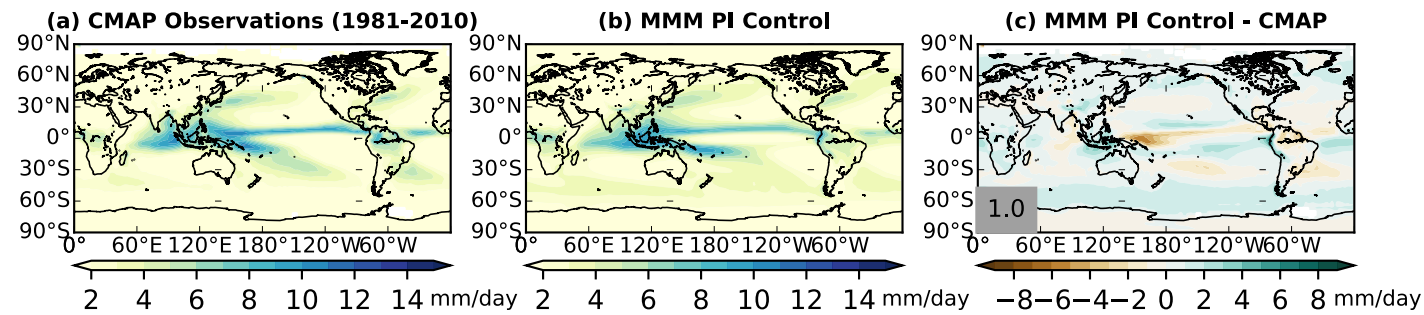


Figure 3.

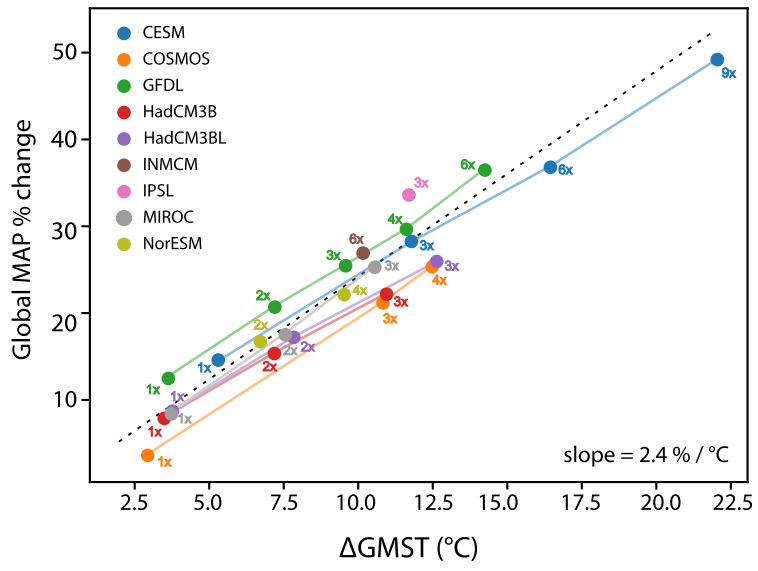


Figure 4.

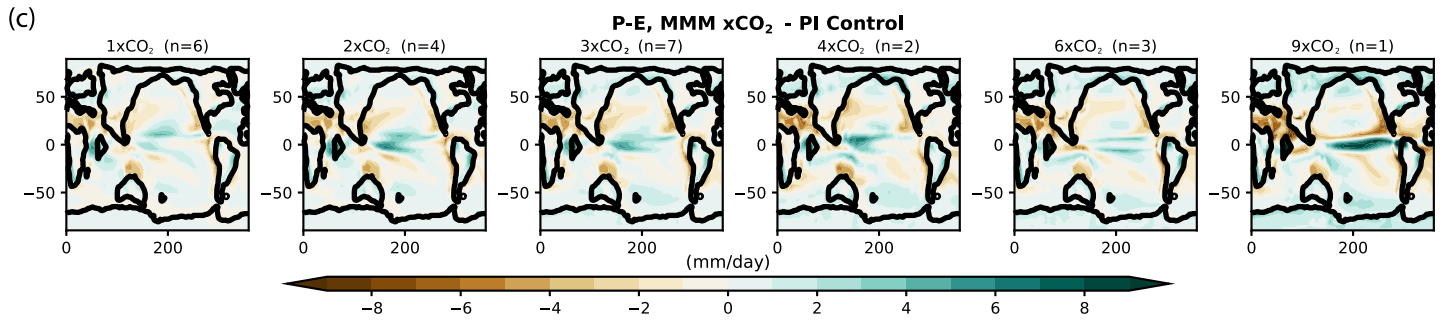
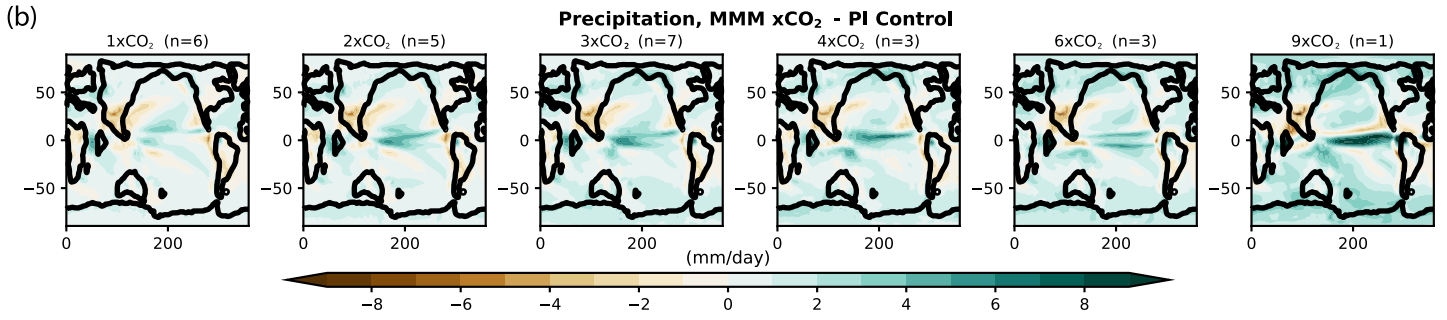
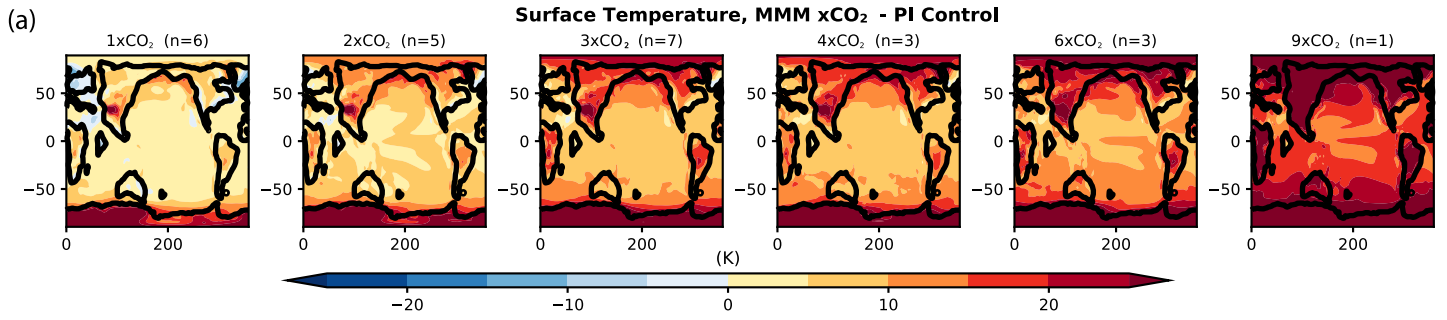


Figure 5.

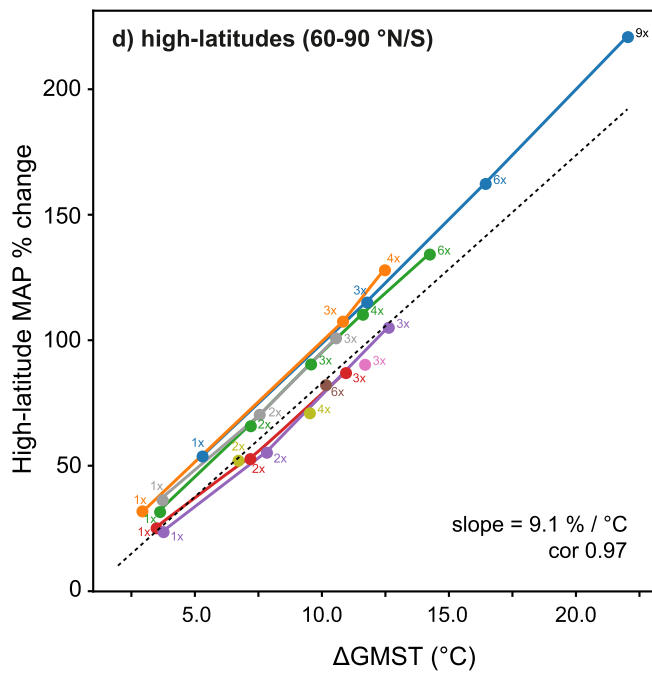
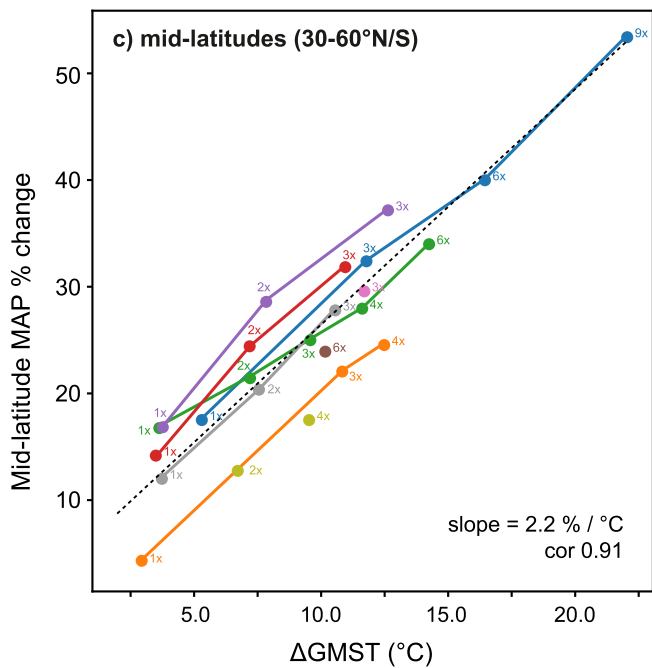
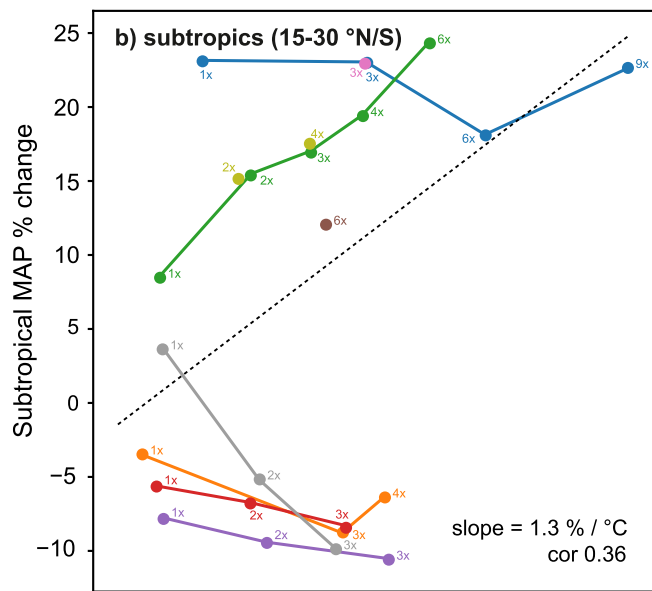
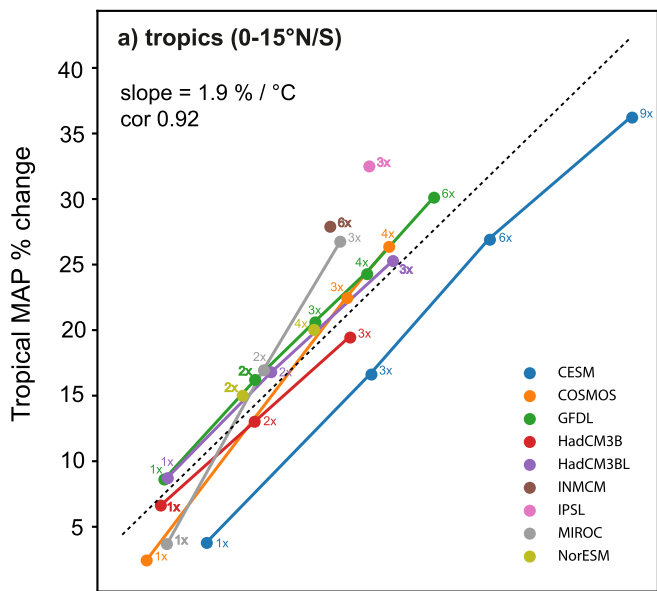


Figure 6.

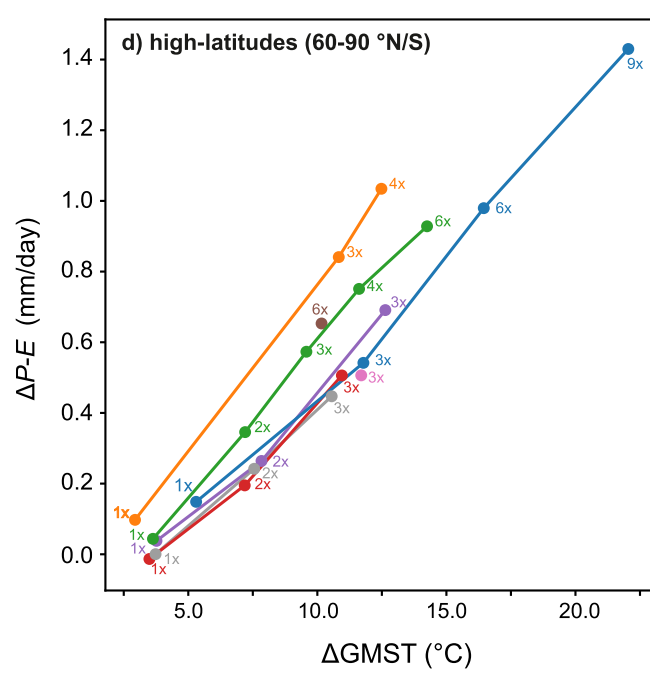
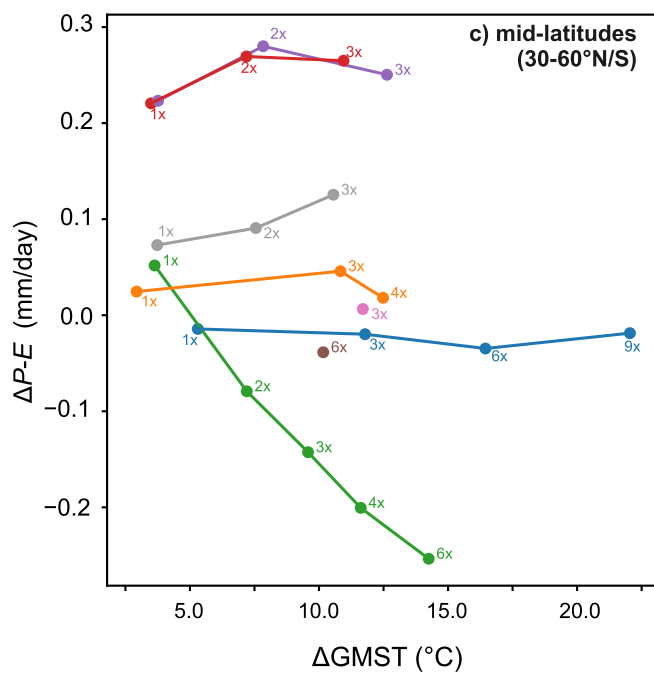
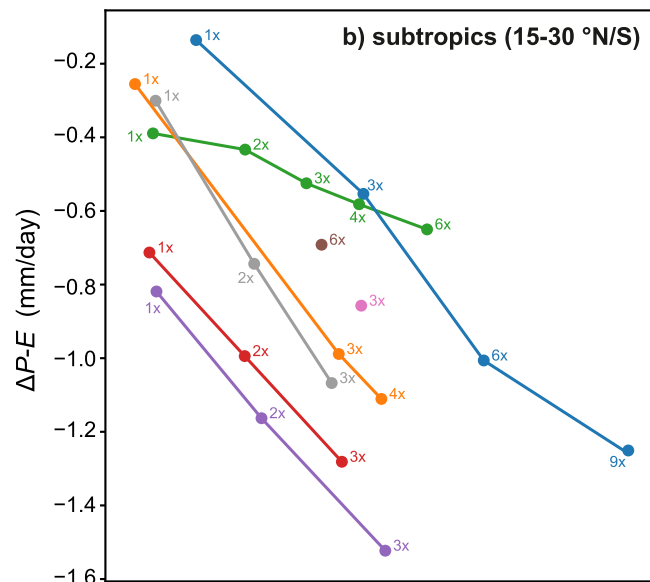
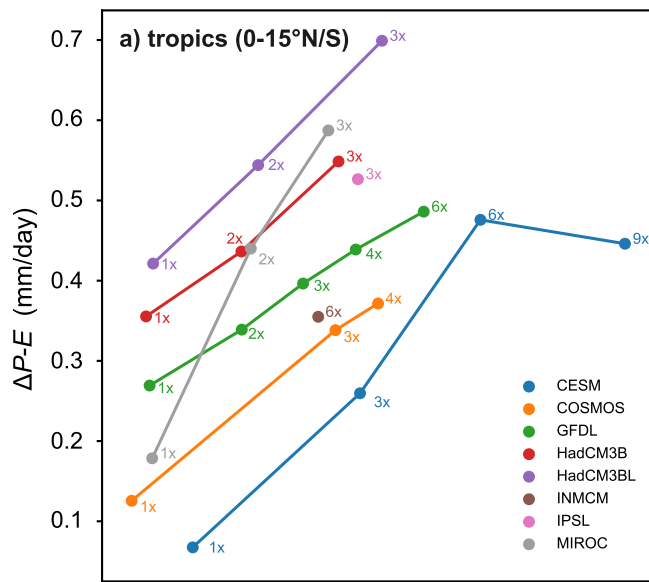


Figure 7.

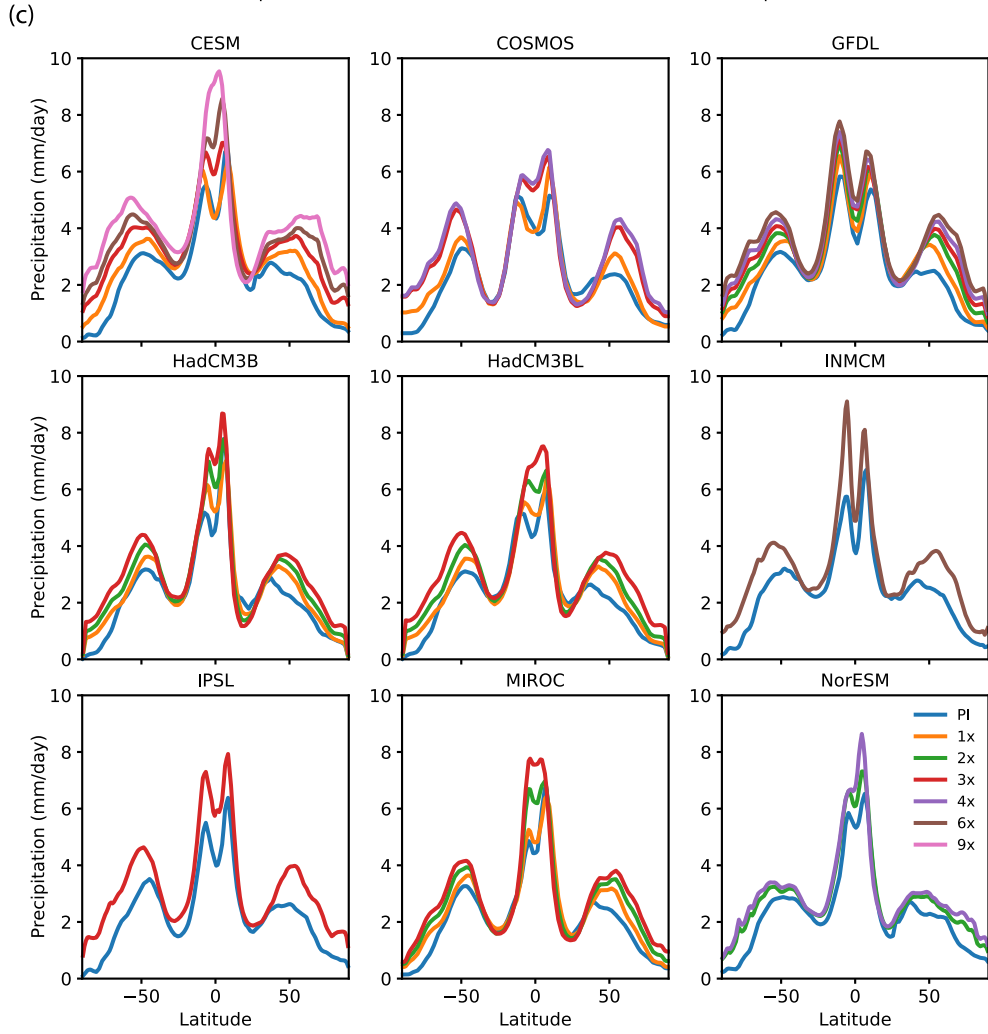
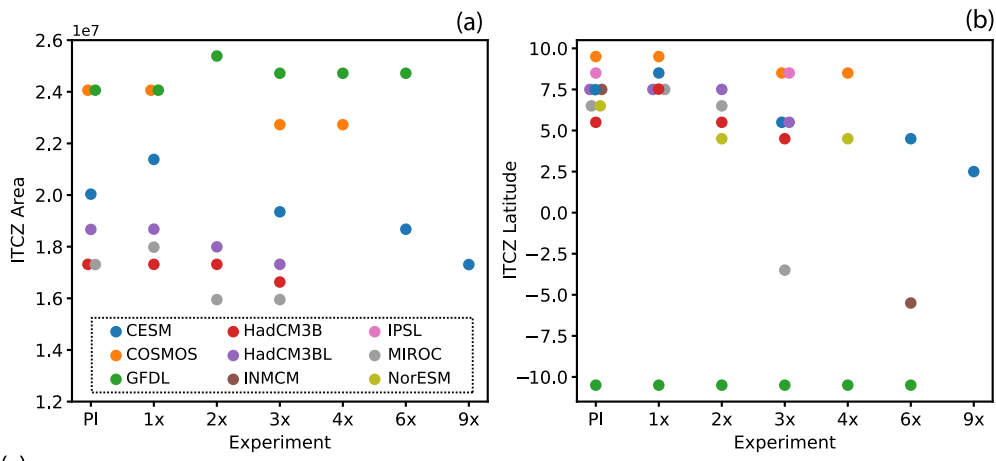


Figure 8.

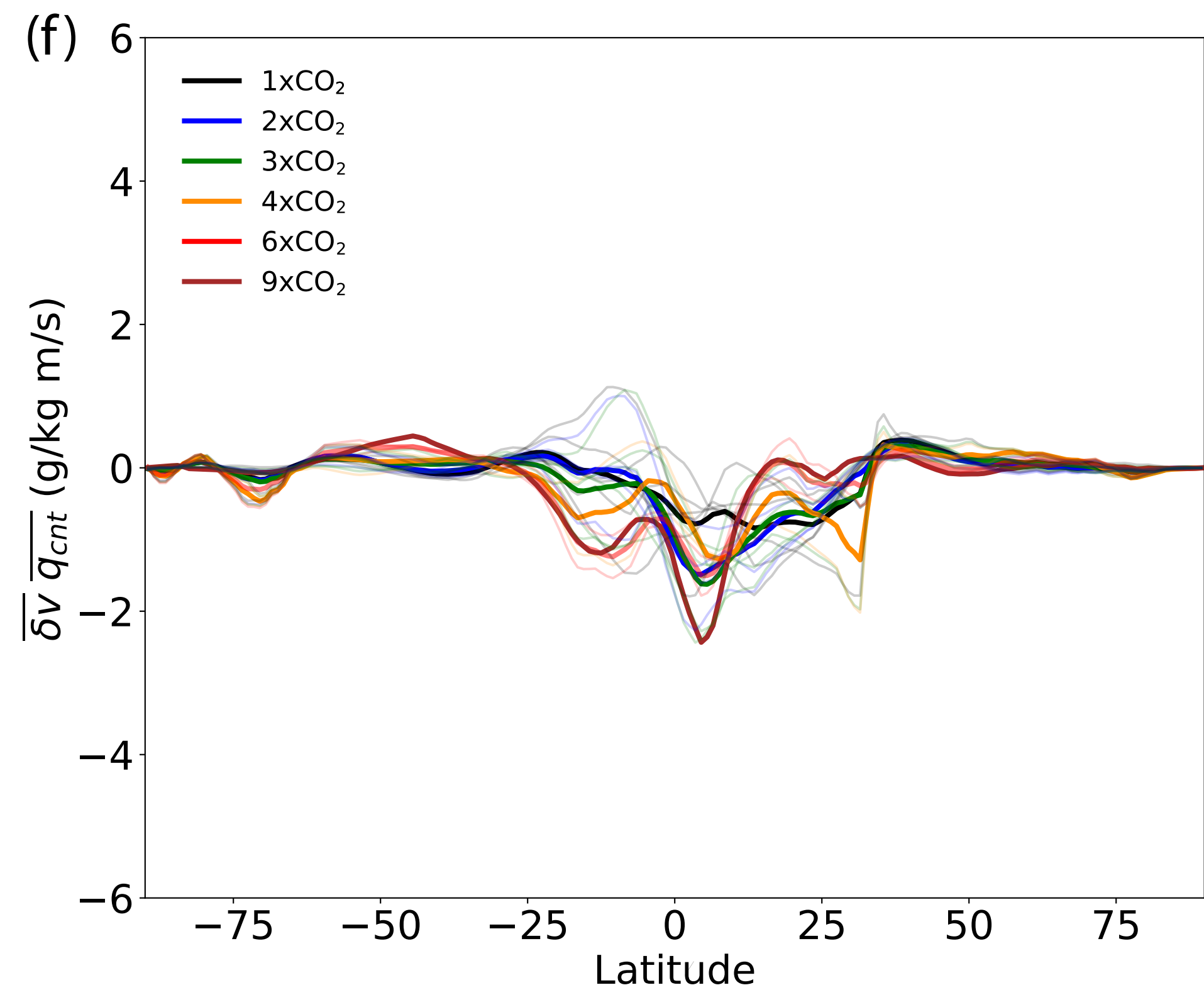
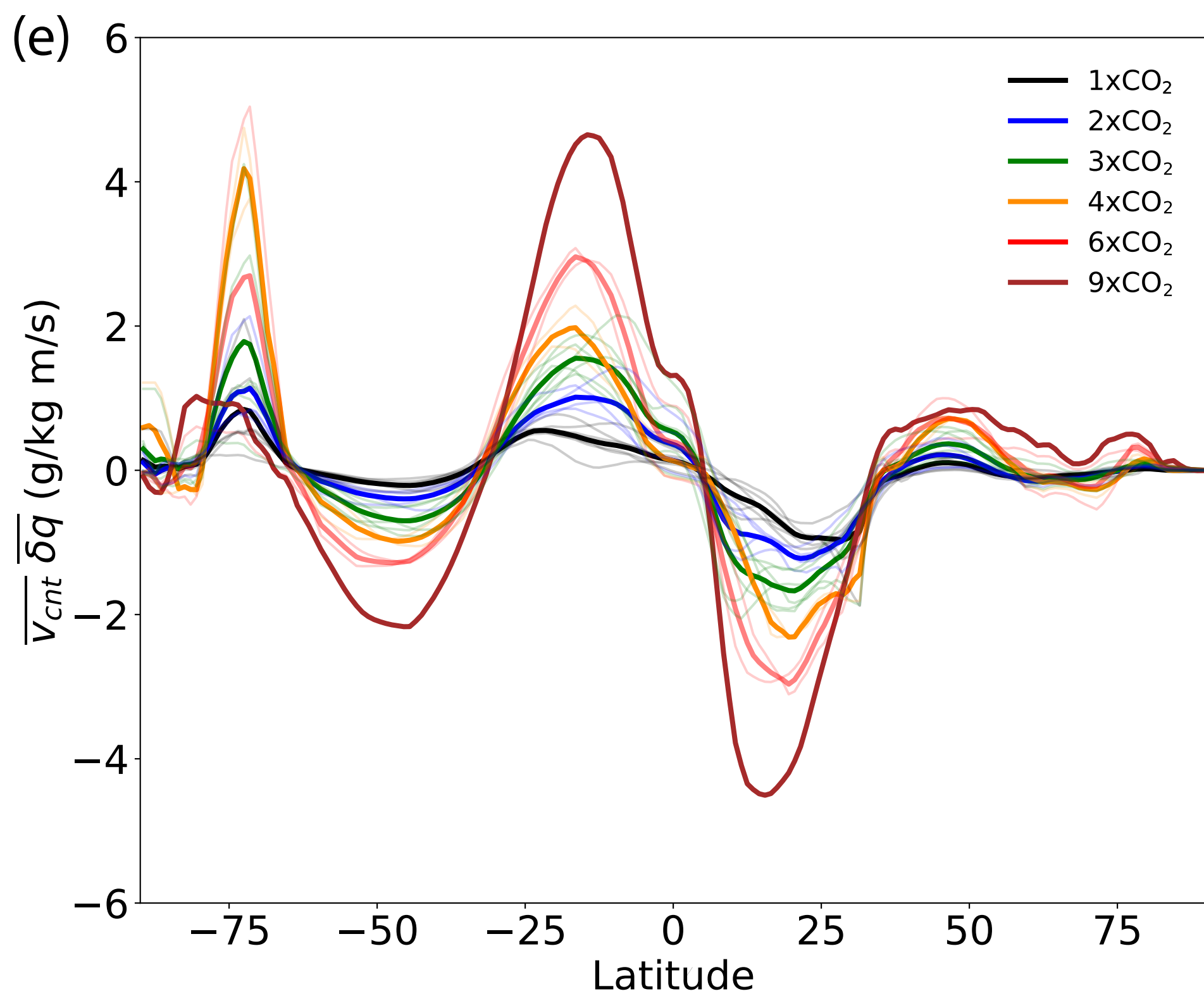
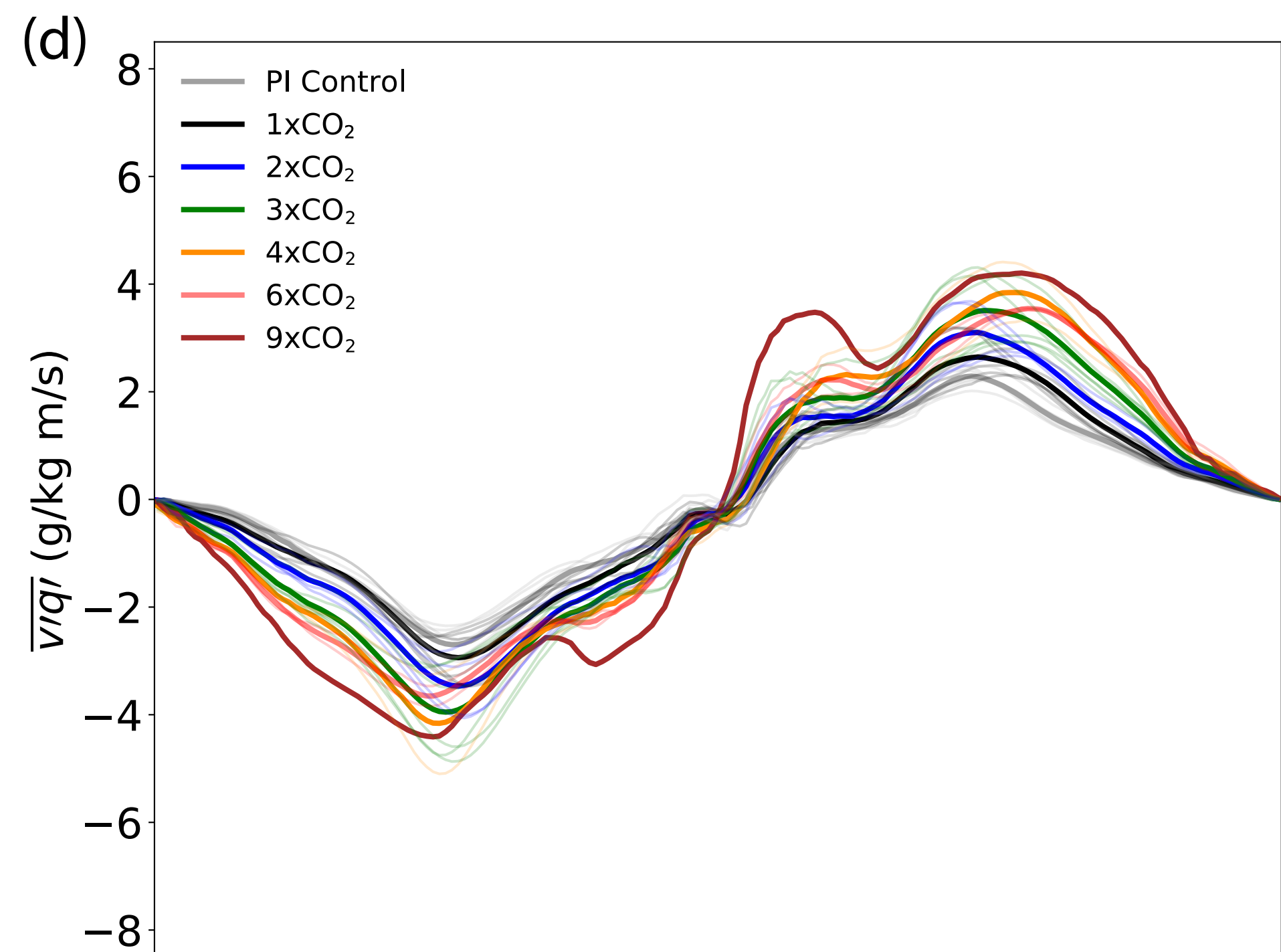
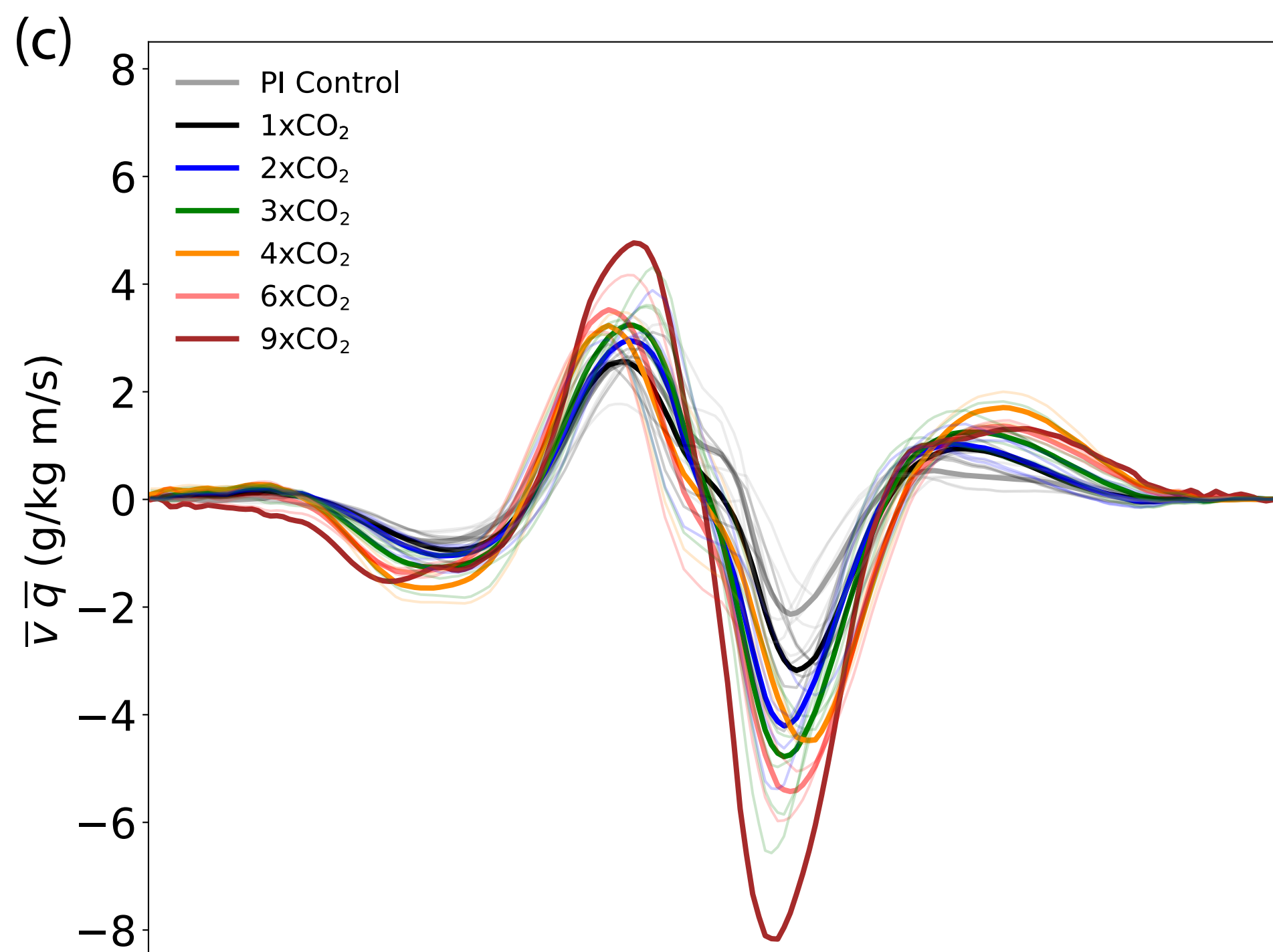
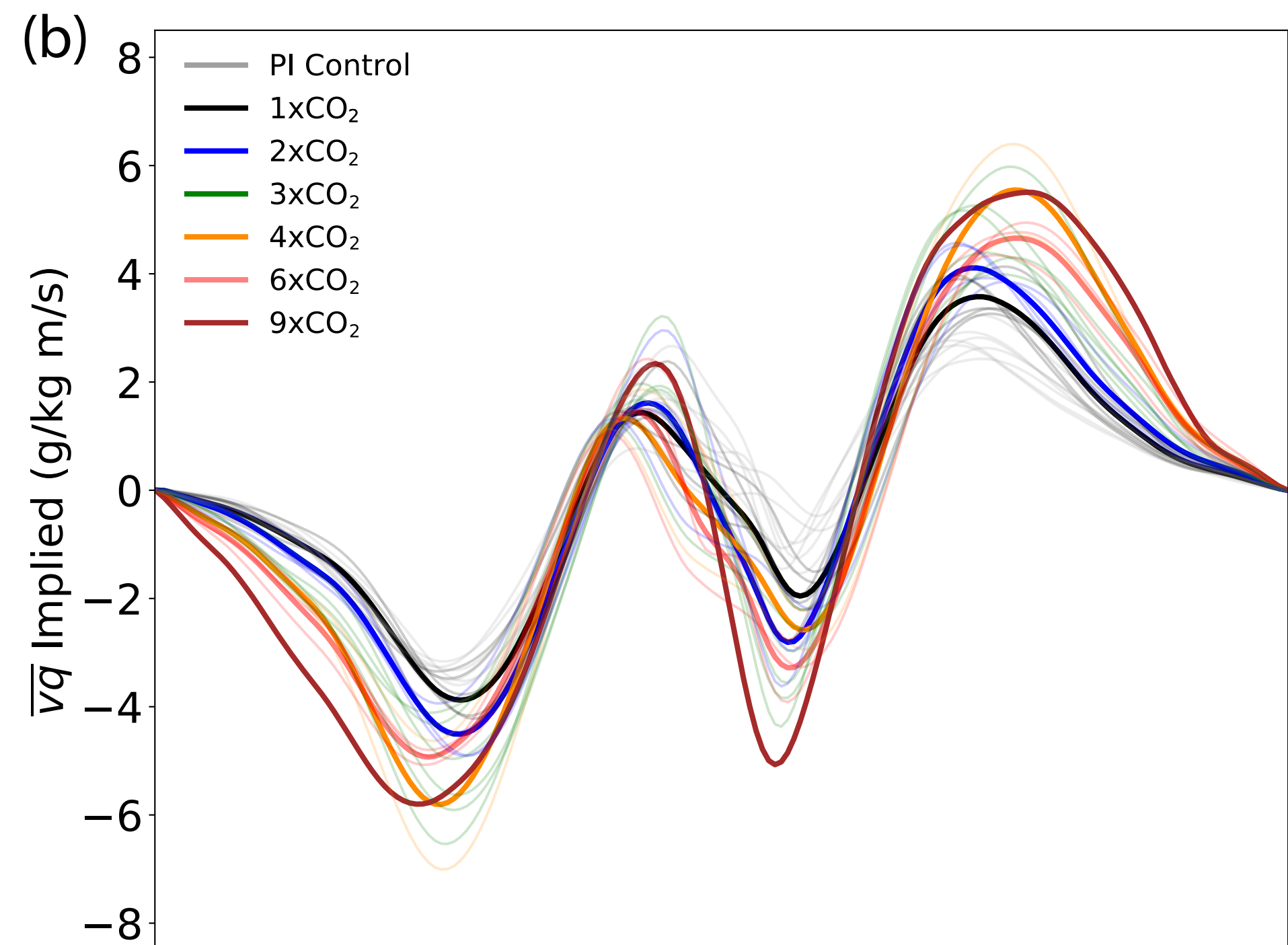
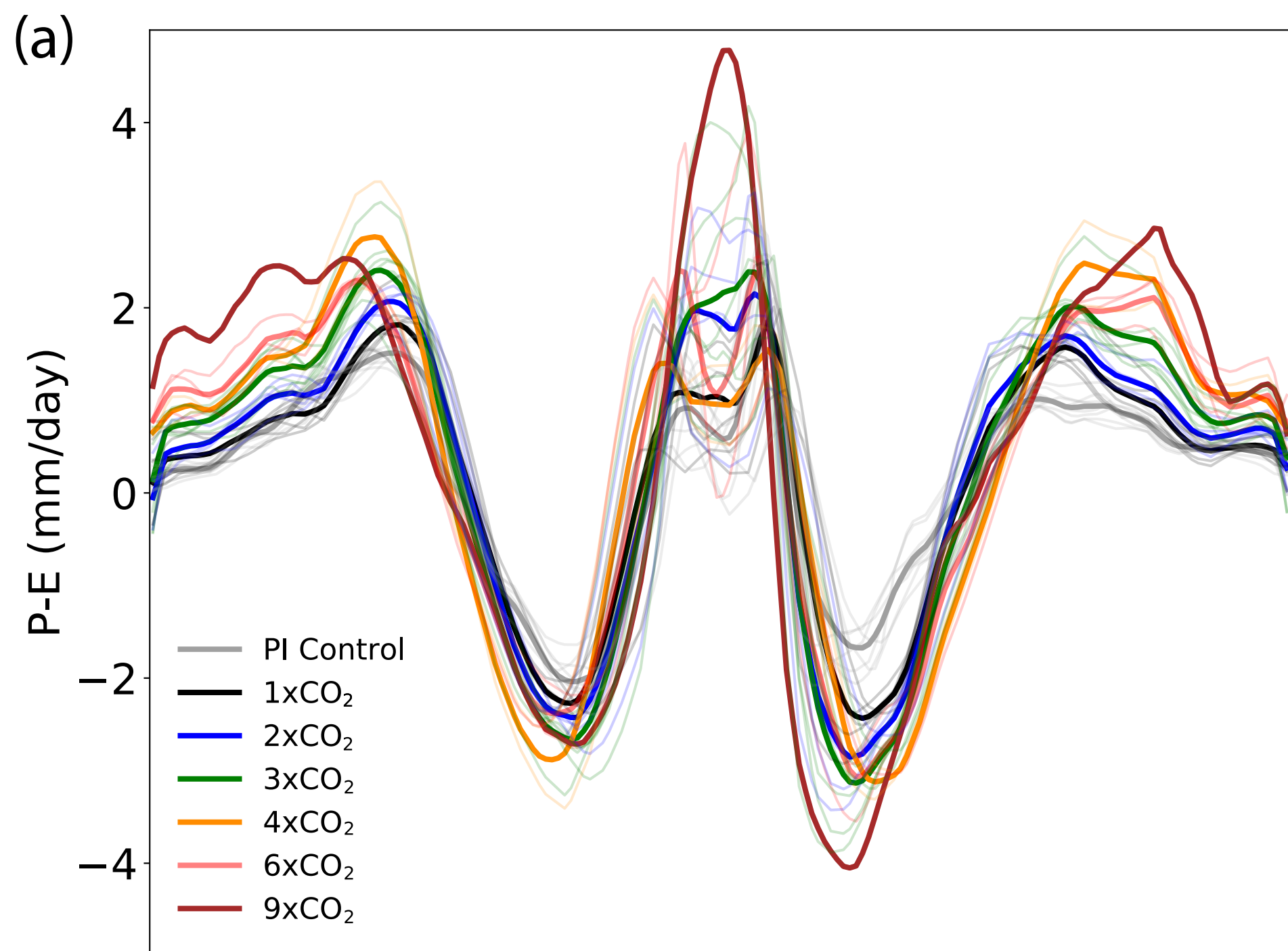


Figure 9.

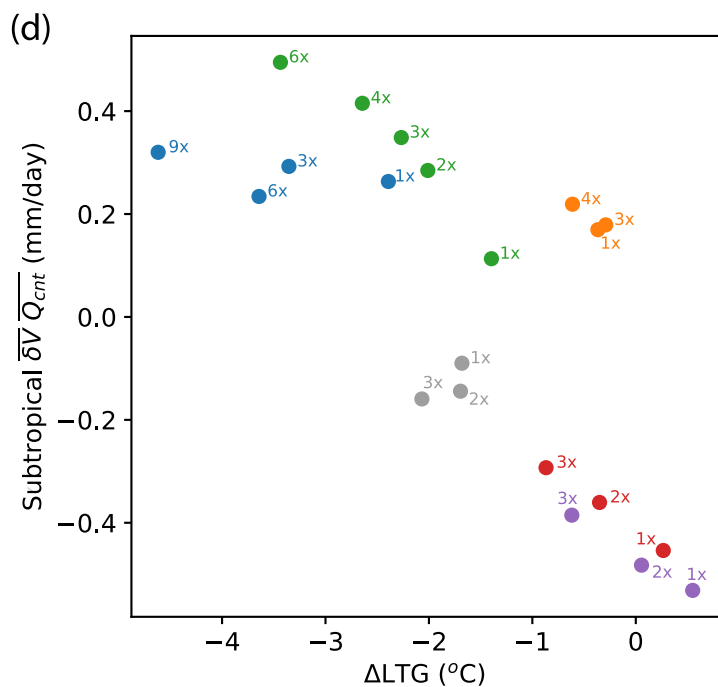
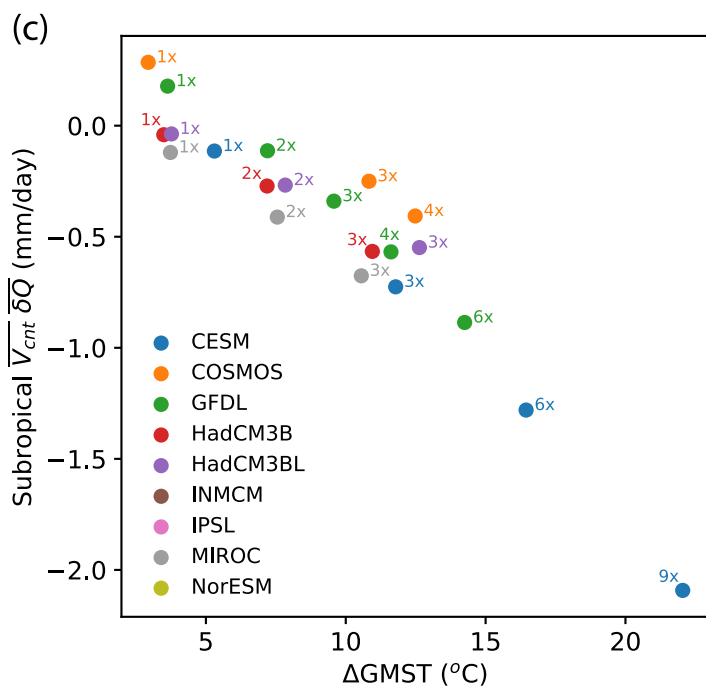
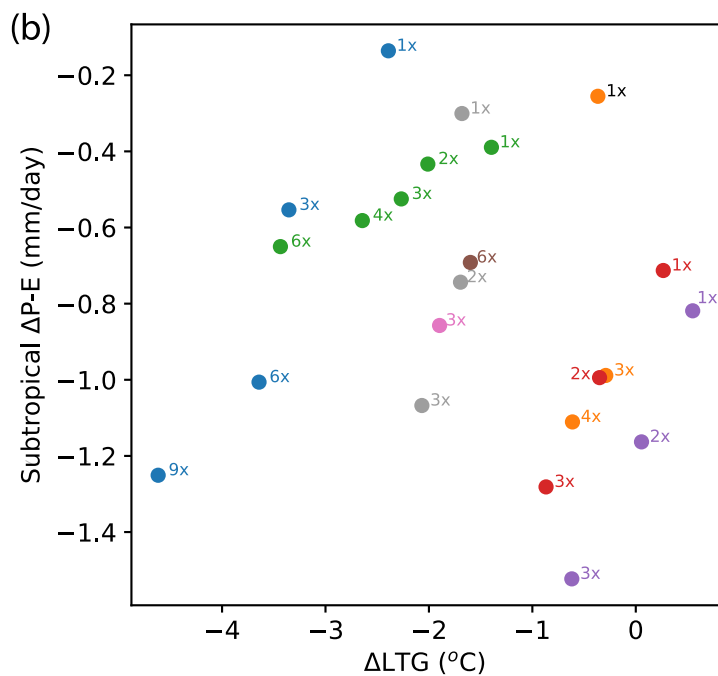
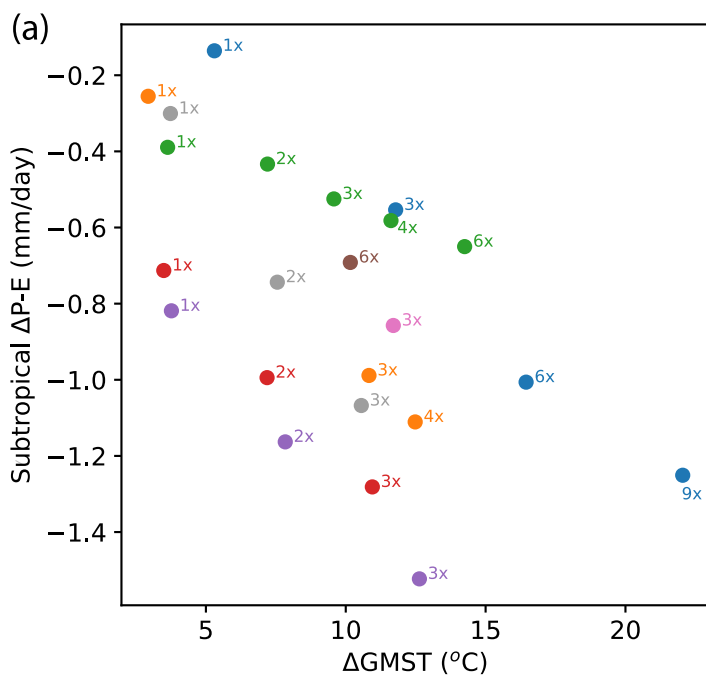


Figure 10.

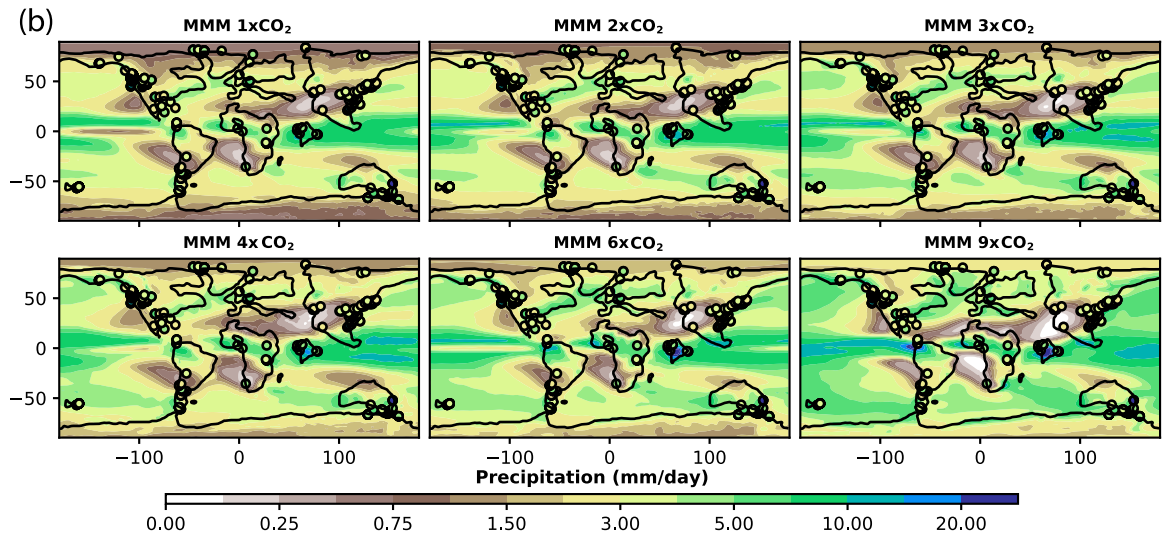
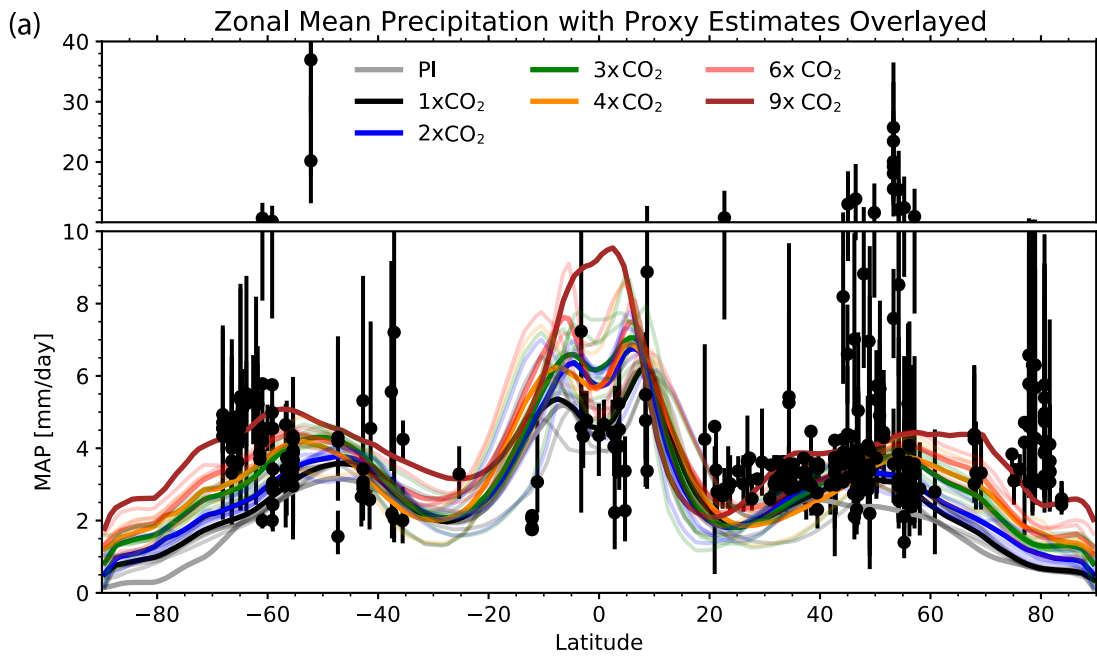
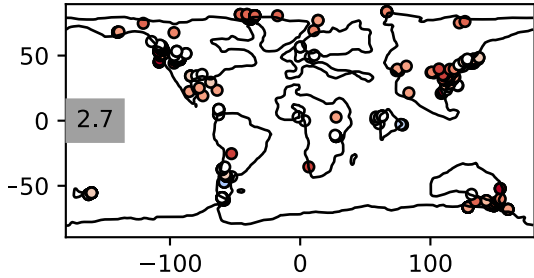
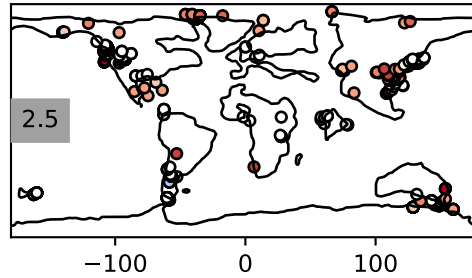


Figure 11.

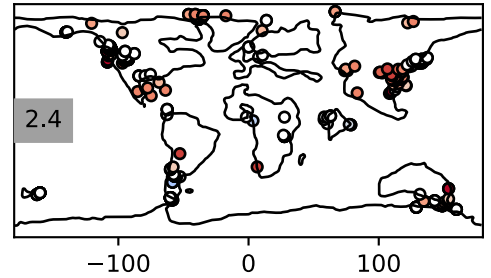
MMM 1xCO₂ (n=6)



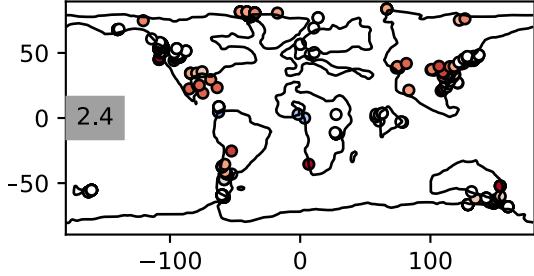
MMM 2xCO₂ (n=5)



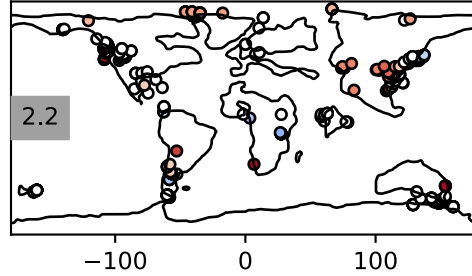
MMM 3xCO₂ (n=7)



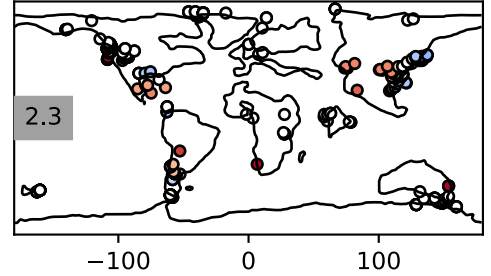
MMM 4xCO₂ (n=3)



MMM 6xCO₂ (n=3)



MMM 9xCO₂ (n=1)



Precipitation Bias (mm/day)

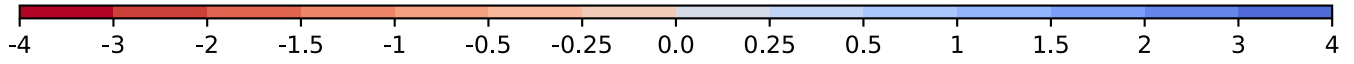


Figure 11.

